Analyzing the Synoptic-, Meso- and Local- Scale Involved in Sea Breeze Formation and Frontal Characteristics

Jon A. Arrillaga, Pedro Jiménez, Jordi Vilà-Guerau de Arellano, Maria A. Jiménez, Carlos Román-Cascón, Mariano Sastre, Carlos Yagüe

JGR Atmospheres

RESEARCH ARTICLE
10.1029/2019JD031302

Analyzing the Synoptic-, Meso- and Local- Scale Involved in Sea Breeze Formation and Frontal Characteristics

Jon A. Arrillaga[1], Pedro Jiménez[2], Jordi Vilà-Guerau de Arellano[3], Maria A. Jiménez[4], Carlos Román-Cascón[5,6], Mariano Sastre[1], and Carlos Yagüe[1]

[1]Departamento Física de la Tierra y Astrofísica, Universidad Complutense de Madrid, Madrid, Spain, [2]Research Applications Laboratory, National Center for Atmospheric Research, Boulder, CO, USA, [3]Meteorology and Air Quality Group, Wageningen University, Wageningen, Netherlands, [4]Departamento de Física, Universitat de les Illes Balears, Palma, Spain, [5]Laboratoire d'Aérologie, CNRS, Université de Toulouse, UPS, Toulouse, France, [6]Centre National d'Études Spatiales (CNES), Toulouse, France

Abstract Sea breeze (SB) frontal passages, the relevant factors influencing their formation and their interaction with local turbulence, are analyzed. To proceed, numerical simulations from the Weather Research and Forecasting (WRF) model are compared with a comprehensive observational database from the Cabauw Experimental Site for Atmospheric Research site, spanning a 10-year period (January 2001 to December 2010). The fine horizontal resolution of 2 km and the replication of the observational vertical levels allow for a more precise comparison. An algorithm based on objective and strict criteria was applied to both observations and simulations to select the SB events. By carrying out a filter-by-filter comparison, we find that the simulated large-scale conditions show a good rate of coincidence with the reanalysis (69%). Small biases in the large-scale wind direction, however, induce important deviations in the surface-wind evolution. Regarding mesoscale forcings, the land-sea temperature gradient is overestimated in average up to 4 K, producing stronger SB fronts in WRF. The analysis of the SB characteristics and impacts is carried out by classifying the events into three boundary-layer regimes (convective, transition, and stable) based on the value of the sensible-heat flux at the SB onset. The stronger SB in the model leads to enhanced turbulence particularly in the convective and transition regimes: The friction velocity, for instance, is overstated by around 50% at the SB onset. In addition, the arrival of the SB front enhances the stable stratification and gives rise to faster afternoon and evening transitions compared with situations solely driven by local atmospheric turbulence.

Key Points:
- Sea breeze onset and direction are markedly biased as a result of deviations in the synoptic-wind direction
- The overestimated sea-land thermal gradient gives rise to stronger sea breeze fronts in the model
- WRF model reproduces greater turbulence after the sea breeze onset and faster afternoon and evening transitions

Correspondence to:
J. A. Arrillaga,
jonanarr@ucm.es

Citation:
Arrillaga, J. A., Jimenéz, P., Vilá-Guerau de Arellano, J., Jiménez, M. A., Román-Cascón, C., Sastre, M., & Yagüe, C. (2020). Analyzing the synoptic scale, mesoscale, and local scale involved in sea breeze formation and frontal characteristics. *Journal of Geophysical Research: Atmospheres*, *125*, e2019JD031302. https://doi.org/10.1029/2019JD031302

Received 4 JUL 2019
Accepted 3 JAN 2020
Accepted article online 25 JAN 2020

Author Contributions
Conceptualization: Jordi Vilà-Guerau de Arellano, Maria A. Jiménez, Mariano Sastre, Carlos Yagüe
Data curation: Pedro Jiménez, Jordi Vilà-Guerau de Arellano, Maria A. Jiménez, Carlos Román-Cascón, Mariano Sastre, Carlos Yagüe
Funding Acquisition: Pedro Jiménez, Jordi Vilà-Guerau de Arellano, Carlos Yagüe
Methodology: Pedro Jiménez, Carlos Román-Cascón, Carlos Yagüe
Software: Pedro Jiménez
Validation: Jordi Vilà-Guerau de Arellano
Formal Analysis: Pedro Jiménez, Jordi Vilà-Guerau de Arellano, Maria A. Jiménez, Carlos Román-Cascón, Mariano Sastre, Carlos Yagüe

1. Introduction

The evolution of the atmospheric boundary layer (ABL) in coastal areas is influenced by the sea breeze (SB) circulation, which is dominant during the warmest months of the year when the synoptic forcing is quiescent and the insolation important. In particular, the SB has been widely investigated due to its influence on the diffusion of pollutants (Borge et al., 2008; Clappier et al., 2000; Papanastasiou, Melas & Lissaridis 2010), the generation of wind energy offshore (Archer et al., 2014; Seroka et al., 2018; Steele et al., 2013), convection and precipitation (Azorín-Molina et al., 2014; Comin et al., 2015), the transport and recirculation of relevant gases (Ahmadov et al., 2007; Gangoiti et al., 2001; Hernádez-Ceballos et al., 2015; Zahorowski et al., 2008), and the forecasting of maximum temperatures in coastal regions during hot spells (Meir et al., 2013; Papanastasiou, Melas, Bartzanas et al., 2010). Around 40% of the population lives within 100 km of the coast (SEDAC, 2019); therefore, the understanding and adequate representation of the SB in mesoscale numerical models are highly relevant.

Numerical experiments have indeed contributed to further understand these mesoscale phenomena, since they provide information about their vertical and spatial extent not covered by the available observations. Mesoscale models, however, fail in reproducing accurately the SB, mainly due to the inadequate representation of turbulence in the ABL (Crosman & Horel, 2010), and in particular the morning (Jiménez, Simó et al. 2016) and afternoon/evening transition periods (Couvreux et al., 2016). In general, little attention has been paid to exploring the impact of the simulated local turbulence on the characteristics of the reproduced sea breeze-front (SBF) passages and, in turn, how local turbulence responds to the arrival of the SBF. Furthermore, despite the SB investigations have frequently been constrained to near-shore areas, the SB has

Investigation: Pedro Jiménez, Jordi Vilà-Guerau de Arellano, Maria A. Jiménez, Carlos Yagüe
Project Administration: Pedro Jiménez, Jordi Vilà-Guerau de Arellano, Carlos Yagüe
Resources: Pedro Jiménez
Supervision: Jordi Vilà-Guerau de Arellano, Maria A. Jiménez, Carlos Román-Cascón, Mariano Sastre, Carlos Yagüe
Visualization: Pedro Jiménez, Jordi Vilà-Guerau de Arellano, Maria A. Jiménez, Carlos Román-Cascón, Mariano Sastre, Carlos Yagüe

been detected as far as few hundred km-s inland (Hu & Xue, 2016; Soler et al., 2014). As a consequence, the inland-progressing SBF encounters evolving local-turbulence conditions, which influence its characteristics as well as its impacts.

In response to the need of a further knowledge about the interconnection between the SB and local-turbulence conditions, Arrillaga et al. (2018) carried out a comprehensive analysis of SB characteristics under different ABL regimes during the afternoon and evening transition (AET). For that, they employed a 10-year observational database from the Cabauw Experimental Site for Atmospheric Research (CESAR) site (the Netherlands), with surface and upper-atmospheric measurements at various vertical levels up to 200 m, providing a complete description of the lower atmosphere. Earlier, Jiménez, de Arellano, et al. (2016) analyzed the contributions to the ABL wind profile by using the same observational database combined with numerical simulations from the Weather Research and Forecasting (WRF) model spanning the 10-year period. They focused on the role of a mesoscale contribution in the wind veering different from the SBF: the near-coastal diurnal acceleration, which occurs prior to the SBF and with a further-inland extent. In this work, and extending the above-mentioned previous investigations, we study in depth the well-defined SBF passages from the numerical simulations. The methodology from Arrillaga et al. (2018) is followed to analyze their representation in the model, focusing on their characteristics and the interaction with turbulence during the AET.

In Arrillaga et al. (2018) the passage of a well-defined SBF is identified, under favorable synoptic and mesoscale conditions, from a sudden shift to an onshore wind direction and the stationarity of the wind vector in this last direction for few hours (Borne et al., 1998). Large databases require a powerful objective technique in order to select SB occurrences based on fixed parameters, so that their analysis is independent of subjective choices. The use of such objective detection methods has been implemented in some investigations. Hughes and Veron (2018), for instance, applied objective algorithms to select SB occurrences from long observational and numerical databases, based on specific criteria for the mesoscale forcings and the frontal wind veering. They employed different techniques to select the events from the observations and from the numerical simulations: In the observations, they compared a station affected and a reference station not affected by the SB, whereas in the simulations, they computed the average wind vector within sample cells. In this work, however, we employ the same algorithm applied to observations to select SB events from the WRF database. In this way, we are able to evaluate how the synoptic, mesoscale, and local forcings that lead to SB formation are represented in the model. There are plenty of investigations that evaluate the relevant influence of for instance the synoptic flow on SB characteristics (Mestayer et al., 2018; Seroka et al., 2018; Steele et al., 2013), but as a result of using fixed thresholds, we infer the existence of systematic biases or patterns giving rise to discrepancy in the model. More adequate representations of these forcings are fundamental to achieve precise forecasts of SB phenomena and their implications in the ABL at coastal regions.

The main goals of this analysis are hence to assess the following:

1. The spatial scales of the physical mechanisms that give rise to consistency or discrepancy in the objective SB selection between the observations and the WRF model.
2. The performance of the WRF model in reproducing the afternoon and evening SBFs and their interaction with turbulence under different ABL regimes.

The robust study of SB occurrences is carried out thanks to the long and complete observational and numerical databases, which allow a consistent validation of the model. This article is structured as follows. Section 2 describes these data and the selection algorithm used to select the SB events. The large-scale, mesoscale, and local forcings influencing the SB detection are evaluated in section 3. In section 4 we analyze the performance of WRF in reproducing the observed SB features for different ABL regimes and their impacts on local turbulence. We finish with the conclusions and future prospects of the analysis.

2. Method

2.1. Data

First, we have an observational database of 10 years (January 2001 to December 2010) from the CESAR in the Netherlands, which is part of the 3-D Ruisdael observational facility (Ruisdael-Observatory, 2019). It is located at approximately 50 km from the sea in a flat area (see Figure 1). Measurements were

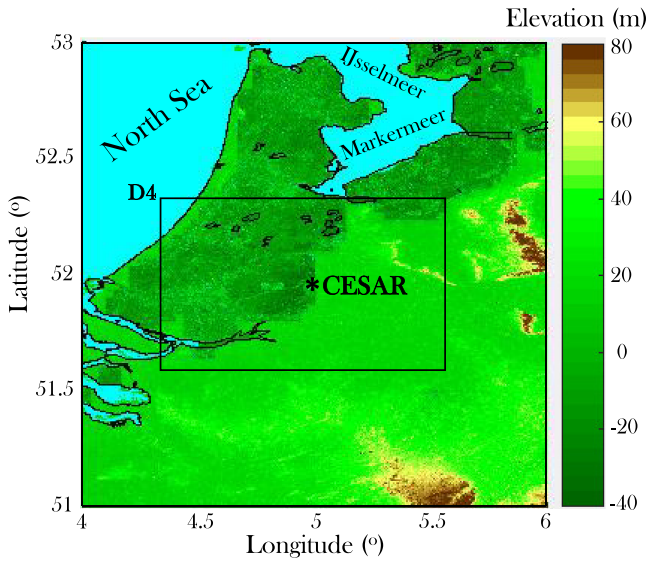

Figure 1. Topographical map of the area surrounding the CESAR site, which is indicated with a black asterisk. The name of the nearby seas and the smallest domain from the numerical simulations (D4) are also shown.

taken at various vertical levels along a 213-m tower (2, 10, 20, 40, 80, 140, and 200 m), with an average time of 10 min. Eddy-covariance measurements were also carried out at different levels, but only the surface-turbulence measurements are validated for the 10-year data. Details about the corrections and postprocessing of high-frequency data are given in Bosveld (2017). Data from the tower are complemented with the mixing-layer height (MLH) from a wind profiler, which estimates the ABL height. Further specifications about this observational database can also be consulted in Arrillaga et al. (2018), from now on AR18.

Numerical simulations from the WRF model spanning the same 10-year period are compared with the observations. In order to carry out an objective comparison, the simulated data corresponding to missing observational data were removed from the 10-year data set. The missing data range from none (0%) in the case of for instance the wind speed to 1.4% in the case of the specific humidity. Moreover, the 10-min observations were adapted to 1-hr time resolution in order to be consistent with the time resolution from the numerical simulations. To prevent smoothing of the observed trends, the adaptation was performed by choosing the hourly observational data, not by calculating hourly means. In particular, within each hourly interval the average value corresponding to the first 10-min window was chosen.

2.2. WRF Model

The model (Version 3.4.1) is configured with four nested domains, which have a three to one spatial resolution (see Jiménez, de Arellano et al., 2016, for further specifications). The outputs of the numerical simulations are recorded every hour, and the smallest domain of the model configuration is centered at the CESAR site (see Figure 1), having a horizontal resolution of 2 km. The distribution of vertical levels (36 in total) is standard, with finer resolution near the surface to follow the observational levels of measurements (6 up to 200 m).

The runs are carried out every 48 hr, with the first 24 hr being the spin-up time. This strategy is adopted with the goal of not deviating considerably from the large-scale conditions prescribed from the ERA-Interim reanalysis at 0.75° × 0.75° resolution, which is employed as initial and boundary conditions in the simulations. Further specifications about the modeling configuration can be found in Jiménez, de Arellano et al. (2016), where the numerical experiment is described. A summary of the model configuration is shown in Table 1.

The employed ABL scheme is YSU, a first-order closure scheme with a countergradient term to account for the nonlocal mixing (Hong et al., 2006). As concluded in the works from Challa et al. (2009), Steele et al. (2013), and Arrillaga et al. (2016), this scheme provides an adequate and less-biased representation of the SB compared to other ABL schemes. Regarding the land-surface model (LSM), the five-layer model

Table 1
WRF Model Setting

WRF configuration and physics	Value	Reference
Central point	51.97° N, 4.93° E	
Horizontal resolution (km)	4 nested domains (54; 18; 6; 2)	
Vertical resolution	36 eta levels (6 in the first 200 m)	
Initial and boundary conditions	ERA Interim (6 h)	
Longwave physics	RRTM (Rapid Radiative Transfer Model)	Mlawer et al. (1997)
Shortwave physics	Dudhia	Dudhia (1989)
Microphysics	WSM-6-class	Hong and Lim (2006)
Surface physics	5-layer model	Dudhia (1996)
ABL scheme	YSU	Hong et al. (2006)

Table 2
Statistical Evaluation of the SB Algorithm Applied to Observations and Numerical Simulations During the 10 Analyzed Years (1,230 Days in Total Corresponding to the Warm Period)

Filter	Description	Variable	#(obs.)	#(WRF)	#(coinc.)	%(coinc.)
1	Synoptic wind	V_{850}	382	377	320	84
2	Synoptic fronts	$\Delta\theta_{e,850}/\Delta t$	326	282	226	69
3	Precipitation	pp	267	202	168	63
4	Thermal gradient	$\Delta T_{sea,land}$	209	201	132	63
5	Frontal passage	$\alpha_{10'}$	75	55	21	28

Note. First column indicates the filter number; second column a short description of each filter; third column the variable evaluated; fourth column the number of days from the observational database that pass each filter; fifth column the number of days from WRF simulations that pass each filter; sixth column the coincident days between the observational and numerical databases; and, finally, seventh column the percentage of the coincident days with respect to the observational database. For further specifications about the criteria of each filter, we refer the reader to AR18

is employed instead of more sophisticated schemes such as Noah (Chen & Dudhia, 2001). The employed LSM is a five-layer soil-temperature model (Dudhia, 1989), which fixes the soil-moisture content for either the extended summer and winter seasons. Before running the 10-year numerical simulation, we carried out sensitivity experiments comparing the performance of the Noah and five-layer LSM-s for few representative case studies (not shown). The results showed that Noah only slightly improved the representation of the sensible-heat (SH) flux under convective conditions, whereas the LH flux was more unadequately reproduced. On the other hand, other works evaluating model parameterizations, in particular the study in a coastal environment from Zhong et al. (2007), shows that the Noah scheme, compared with the five-layer scheme, does not result in better predictions of the PBL structure, its evolution, and the developing local circulations. More specifically, worse predictions of the turbulent fluxes are obtained. A more biased representation of the LH flux with the Noah scheme is also found in the study from Sastre et al. (2015). Hence, for climatological or semiclimatological studies such as the present study it is useful employing a rather simple LSM.

2.3. SB Selection

SB days are selected by employing the SB algorithm defined in AR18, which applies to data five different filters based on objective criteria. Filters 1 and 2 evaluate the synoptic conditions at the level of 850 hPa. The first one assures that the wind speed does not exceed 6 m/s, and the second one evaluates the equivalent potential temperature to discard the days that show a synoptic cold-front passage (a decrease greater than 1.5 K in 6 hr). Filters 3 and 4 apply to mesoscale factors at the surface: The former rejects the days in which precipitation is greater than 0.1 mm, and the latter assures that a minimum sea-land temperature gradient is exceeded (2 K). Finally, Filter 5 requires a local wind veering to an onshore direction followed by a period of a slight variability around that direction, identified as the frontal passage. All the specifications about each filter are provided in AR18.

The same criteria are applied to observations and WRF simulations. In that way, the SB databases obtained from the model and observations are comparable in a consistent way. Besides, the comparison enables us to analyze which factors, either related with the synoptic scale, mesoscale, or local scale, are responsible for the differences revealed. The filtering is carried out in the warm period (May, June, July, and August), when the land-sea temperature difference is large enough as to produce these mesoscale phenomena (Jiménez, de Arellano et al., 2016), provided that synoptic conditions are not dominant. By exploring each filter individually, we are able to distinguish how the different meteorological conditions influence the SB formation. The comparison of the WRF simulations with the observations helps in identifying which processes and interactions are adequately reproduced, which can lead to improved forecasts in numerical weather prediction models.

3. Factors Affecting the SB Detection

The algorithm is applied to the variables obtained from WRF using the same thresholds from AR18. We show in Table 2 the statistics of how each filter of the algorithm performs when applied to both observations and

Table 3
Number of BR, CC, WR, and OR Days in Each Filter

Filter	#BR (%)	#CC (%)	#WR (%)	#OR (%)
1	791 (64%)	320 (26%)	62 (5%)	57 (5%)
2	23 (7%)	226 (64%)	72 (20%)	33 (9%)
3	29 (10%)	168 (44%)	51 (18%)	30 (11%)
4	1 (1%)	132 (69%)	0 (0%)	57 (30%)
5	76 (34%)	21 (9%)	70 (31%)	58 (26%)

Note. BR = both rejected; CC = coincident; WR = WRF rejected; OR = observations rejected. The percentages with respect to the sum of all the events for each filter are also shown.

WRF. All synoptic/large scale, mesoscale, and local (with a spatial scale of few km or less) factors, as well as the representation of the physical processes in the model, are responsible for the differences observed.

The filter-by-filter comparison for the different factors is carried out by analyzing four groups of events: the coincident (CC) days, that is, the coincident days that pass each filter in the observational and numerical databases; the observations-rejected (OR) days, that is, the days that are rejected by the observations but pass the filter in the simulations; the WRF-rejected (WR) days, that is, the days that are rejected in the numerical database but pass the filter in the observations; and, finally, the both-rejected (BR) days, that is, the days that are rejected by both numerical and observational databases in each filter. The number of days resulting for each group in each filter is indicated in Table 3. Note that the CC days (Column 3 in Table 3) are included in the sixth column in Table 2.

3.1. Synoptic Scale

After applying the first two filters, which are related to the synoptic scale, around 69% of the filtered days are CC. This result reveals that the simulated large-scale conditions are slightly biased with respect to the large-scale conditions from the reanalysis. ERA-Interim reanalysis is employed in the observations to account for the large-scale conditions at 850 hPa, which has a horizontal resolution of $0.25° \times 0.25°$. Note that the same reanalysis is used as initial and boundary conditions for the numerical simulations (see Table 1), but in this case with a $0.25° \times 0.25°$ resolution, in contrast to the $0.75° \times 0.75°$ resolution employed for the model initialization. The outputs of the numerical simulations from Domain 2 are employed for the comparison with the reanalysis in Figures 2–5, since they have the closest horizontal resolution (18×18 km) to that of the reanalysis.

To analyze whether the rejection/acceptance in Filter 1 is associated with consistent spatial patterns, we represent in Figure 2 composite maps of the wind speed at 850 hPa for the BR, CC, WR, and OR days. Averages are calculated considering the daytime values from the reanalysis (6, 12, and 18 UTC). Figure 3 shows the wind roses at 850 hPa for the same group of events, also considering the values at 6, 12, and 18 UTC.

In the BR days (791 in total) the spatial pattern that gives rise to rejection ($V_{850} > 6$ m/s) is very similar in the reanalysis and WRF simulations (Figures 2a and 2b), with a maximum wind speed of up to 10 m/s in the dutch coast and prevailing WSW directions (Figures 3a and 3b). The variability of the wind speed is also high, with a standard deviation of up to 5–6 m/s. In these situations dominated by the intense synoptic wind, the SBF does not reach Cabauw, and the thermally driven winds are masked by the large scale. In fact, the resolution of the model is enough to describe realistically the coastal wind pattern in the lower atmosphere. WRF simulations also show a good correspondence with the observations for the 320 CC days (Figures 2c and 2d). An average wind speed minimum of around 4 m/s results in the area surrounding Cabauw, with a small standard deviation, illustrating the consistency of this spatial pattern. These days represent the situations with the weakest large-scale wind in Cabauw and are well illustrated in the reanalysis and WRF simulations. The wind direction is variable and with approximately equal frequencies of all the directions (Figures 3c and 3d). The 62 WR days, however, show contrasting spatial patterns. The reanalysis data display a wind-speed minimum in the area of Cabauw (Figure 2e), not as clear as in the CC days, but in any case contrasting with the local maximum (of up to 7.5 m/s in Cabauw) that is observed in the WRF database. The standard deviation is also slightly greater (~1 m/s) in the model. With respect to the wind directions,

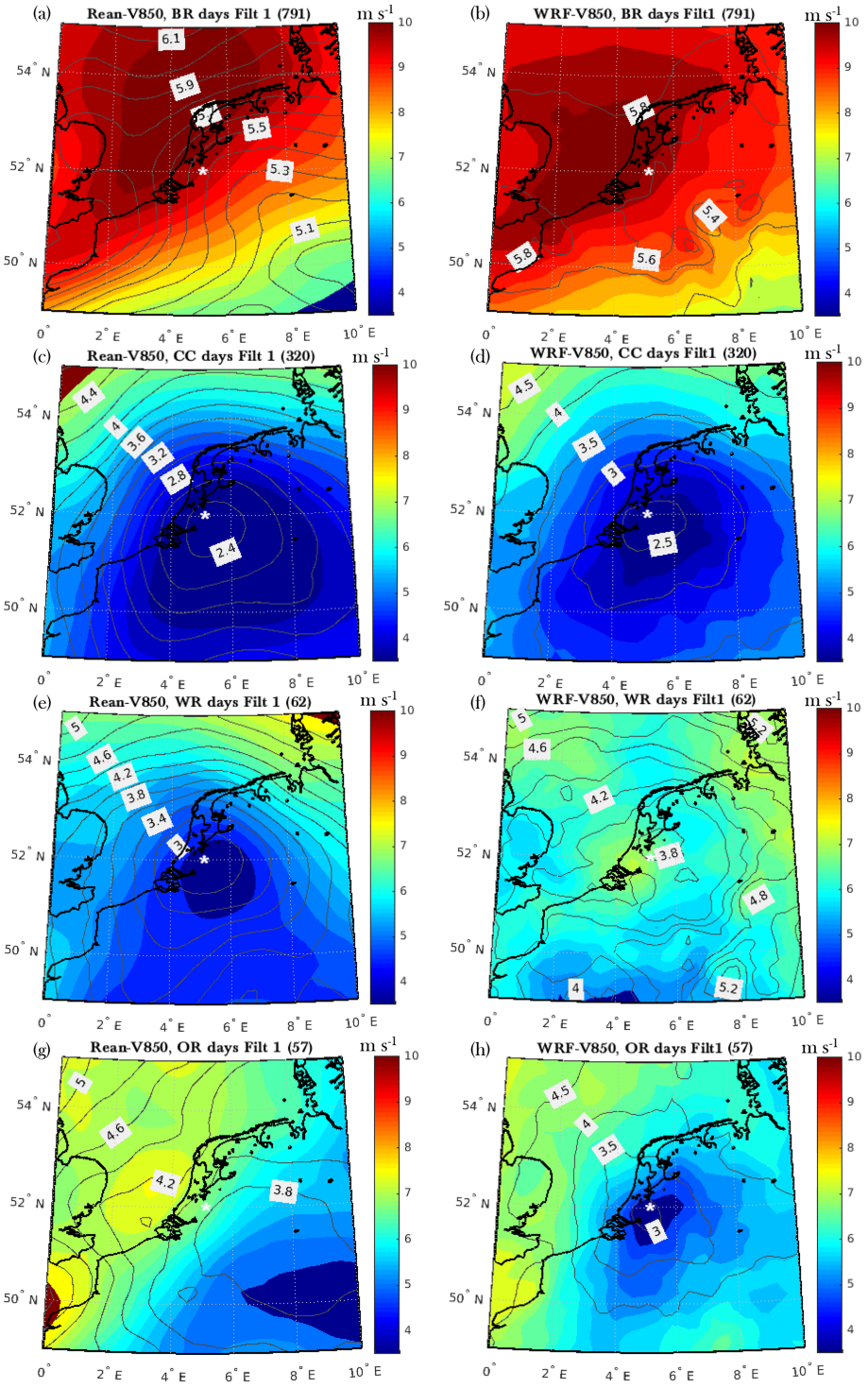

Figure 2. Composite maps of the wind speed at 850 hPa, from reanalysis data (left) and WRF simulations (right), for different groups of events: both-rejected (BR), coincident (CC), WRF-rejected (WR), and observations-rejected (OR) days in Filter 1. The averages are computed from the values at 6, 12, and 18 UTC. The number of events of each group is included in brackets. The gray contours with the labels represent the standard deviation of the composites.

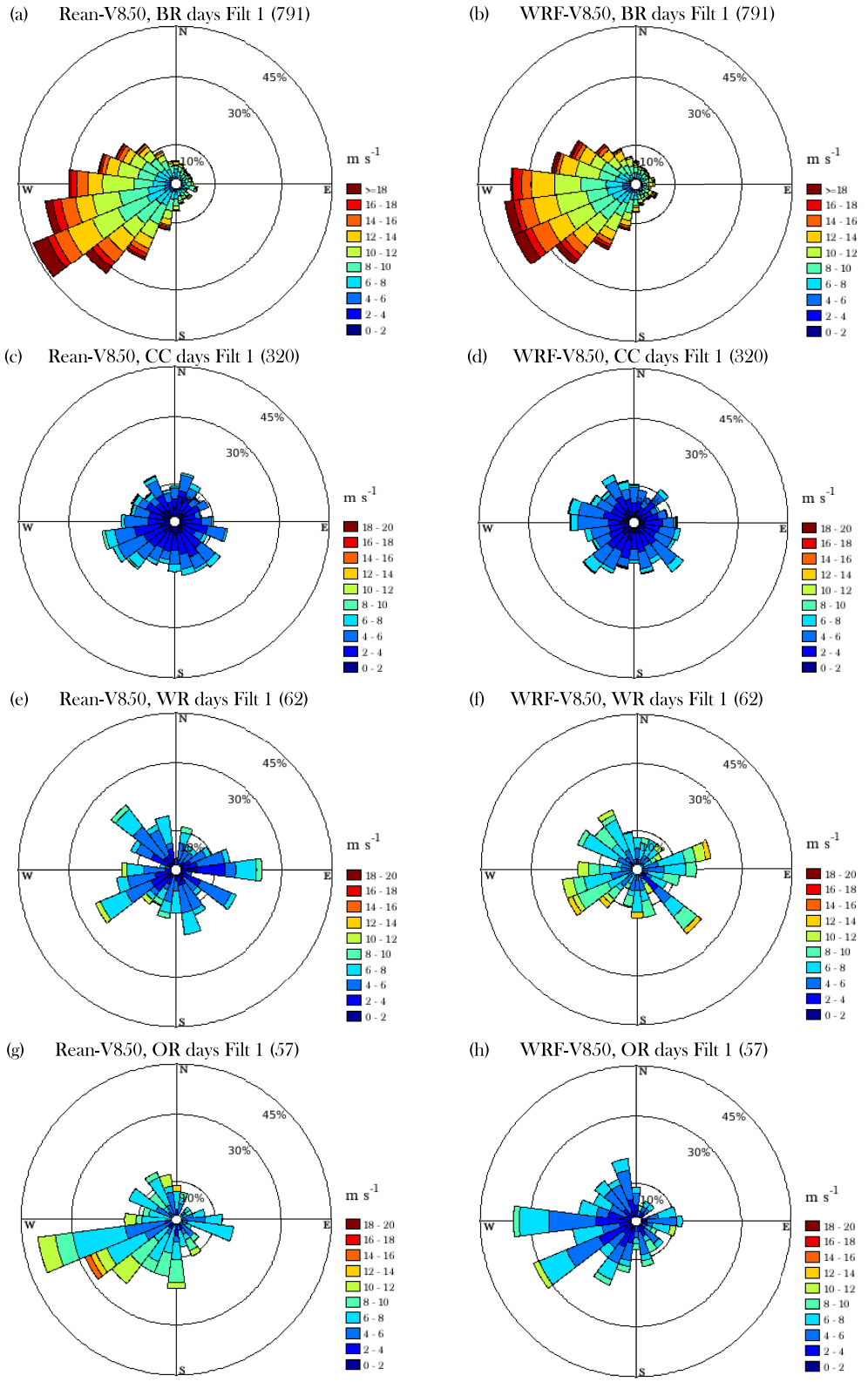

Figure 3. Wind roses at 850 hPa, from reanalysis data (left) and WRF simulations (right), for different groups of events: both-rejected (BR), coincident (CC), WRF-rejected (WR), and observations-rejected (OR) days in Filter 1. Note that they represent values at 6, 12, and 18 UTC. The number of events of each group is included in brackets.

they are very similar in the reanalysis and the model. On the other hand, the WRF database shows a local wind-speed minimum in the area of Cabauw on the 57 OR days, which is not displayed by the reanalysis. The reanalysis, in fact, shows a wind speed in Cabauw, which is very close to the threshold for this filter (6 m/s), with a slightly greater standard deviation (≃1 m/s). The directions, again, show a fair correspondence. In this case, however, the SW directions prevail, with evident stronger intensities in the reanalysis. Therefore, the discrepancy of the model in this filter seems to arise from almost equally frequent overestimations (for WR) and underestimations (for OR) of the large-scale wind of up to 2 m/s in average, even though the representation of the large-scale wind is in general adequate. In fact, the percentage of CC-BR days (90%) is markedly greater than of WR-OR days (10%), as can be noticed from Table 3. Hughes and Veron (2018) also reported occasional misrepresentation of synoptic features in their WRF simulations of SB events.

Rejection in Filter 2 is given by decreases in the equivalent potential temperature at 850 hPa ($\theta_{e,850}$) greater than 1.5 K in 6 hr, associated with the passage of cold synoptic fronts. Figure 4 shows composite maps of the daily minimum decrease of this magnitude in 6 hr (either from 6 to 12 or 12 to 18 UTC) for the BR, WR, OR, and CC days, both from the reanalysis and WRF database. In the 23 BR days the spatial pattern giving rise to the rejection is similar both in reanalysis and WRF, while in the model the decrease in $\theta_{e,850}$ around Cabauw is greater (−4 vs. −3 K per 6 hr) and more extended toward the North Sea than in the reanalysis. The standard deviation is also greater (3 vs. 2 K per 6 hr). The trend of this variable is positive in the CC days for both databases, slightly higher in the reanalysis over the continent (Figure 4c). In the WR and OR days, however, the spatial patterns differ substantially. First, in the days that are rejected by WRF but not by the reanalysis (72 in total, Figures 4e and 4f), $\Delta\theta_{e,850}$/6 hr is around −3.5 K per 6 hr at Cabauw in the model database, although the negative spatial pattern is not as intense as in the BR days (Figure 4b). In the reanalysis, the negative pattern (weaker than in the model) is represented over the North Sea, but not reaching the continental area of Cabauw. This suggests that WRF is simulating forward the passage of the cold fronts. The pattern is reversed in the 33 OR days (Figures 4g and 4h), but in this case the decrease in $\Delta\theta_{e,850}$ is more localized in the reanalysis, while the pattern around Cabauw is unclear in the model. Indeed, the average in the grid point of Cabauw is above −1.5 K per 6 hr, but it is surrounded by lower values particularly toward the North Sea. It suggests, therefore, that the manifestation of the cold front in this variable is somewhat misrepresented in WRF. It must be noted also that the number of WR days is considerably greater than the number of OR days. The comparison shows that the model tends to overestimate the decrease in $\theta_{e,850}$, overestimating consequently the passage of cold synoptic fronts (95 vs. 56).

3.2. Mesoscale

The third filter discards days in which precipitation is greater than 0.1 mm in Cabauw. Since situations dominated by the synoptic scales are rejected in the two previous filters, exclusion in this filter occurs mainly due to convective mesoscale rainfall. The impact of the third filter is greater in WRF: It rejects 28% of the days (80 in total), contrasting with the 18% (59 in total) from the observations. For this filter we just analyze the recorded/simulated precipitation in Cabauw, since the spatial distribution of the precipitation is meaningless for the SB selection. A bias in the estimated precipitation from WRF has also been found in previous studies; for instance, Bughici et al. (2019) related this bias with the misrepresentation of the wind speed, which influences the evapotranspiration and, consequently, the simulated precipitation. The bias in our case could therefore be influenced by the poor representation of the surface-layer physics in Cabauw.

From the rejected days, 29 are BR days, that is, rejected by both databases. In those days, daily-accumulated precipitation is slightly underestimated in the model: (4.3 ± 2.2) mm versus (6.2 ± 5.4) mm. From the 80 days rejected in total in WRF, 10 are within the OR days from Filter 2. In other words, almost 1/3 of the days that were rejected by the reanalysis but not by the WRF simulations in the second filter are rejected in this third filter. Hence, Filter 3 also works discarding the events with cold fronts that were misrepresented by $\theta_{e,850}$ in the model. Interestingly, in these 10 days, precipitation is significantly overestimated in the model: (7.8 ± 2.9) mm versus (1.8 ± 1.4) mm. Moreover, 25 events from 80 are rejected by WRF but not by the observations so far (in the first three filters of the algorithm), with an average daily-accumulated precipitation of (3.1 ± 1.7) mm in the model. On the other hand, 13 from the 59 days rejected in the observations are within the 72 WR days in Filter 2. This result implies that few cold-frontal days may also be poorly represented by $\theta_{e,850}$ in the reanalysis, which are eventually discarded in Filter 3. As occurred with the model, in this case the accumulated precipitation is significantly greater in the observations: The average daily precipitation is of (8.0 ± 8.5) mm in the observations and of (2.2 ± 1.3) mm in WRF. Finally, only 4 from 59 are rejected by

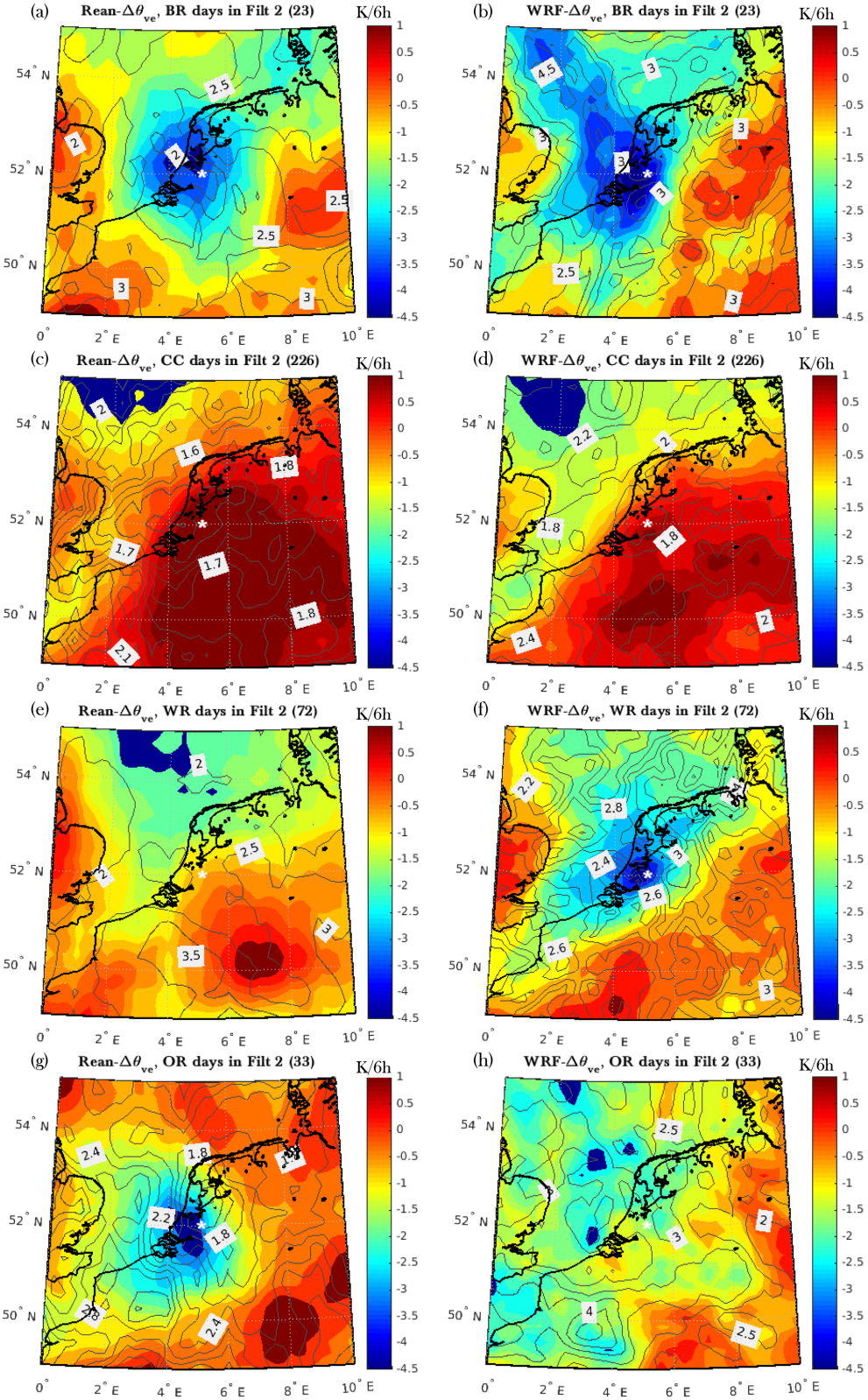

Figure 4. Composite maps of $\Delta\theta_{e,850}$, from reanalysis data (left) and WRF simulations (right), for different groups of events: both-rejected (BR), coincident (CC), WRF-rejected (WR), and observations-rejected (OR) days in Filter 2. The number of events of each group is included in brackets. The gray contours with the labels represent the standard deviation of the composites.

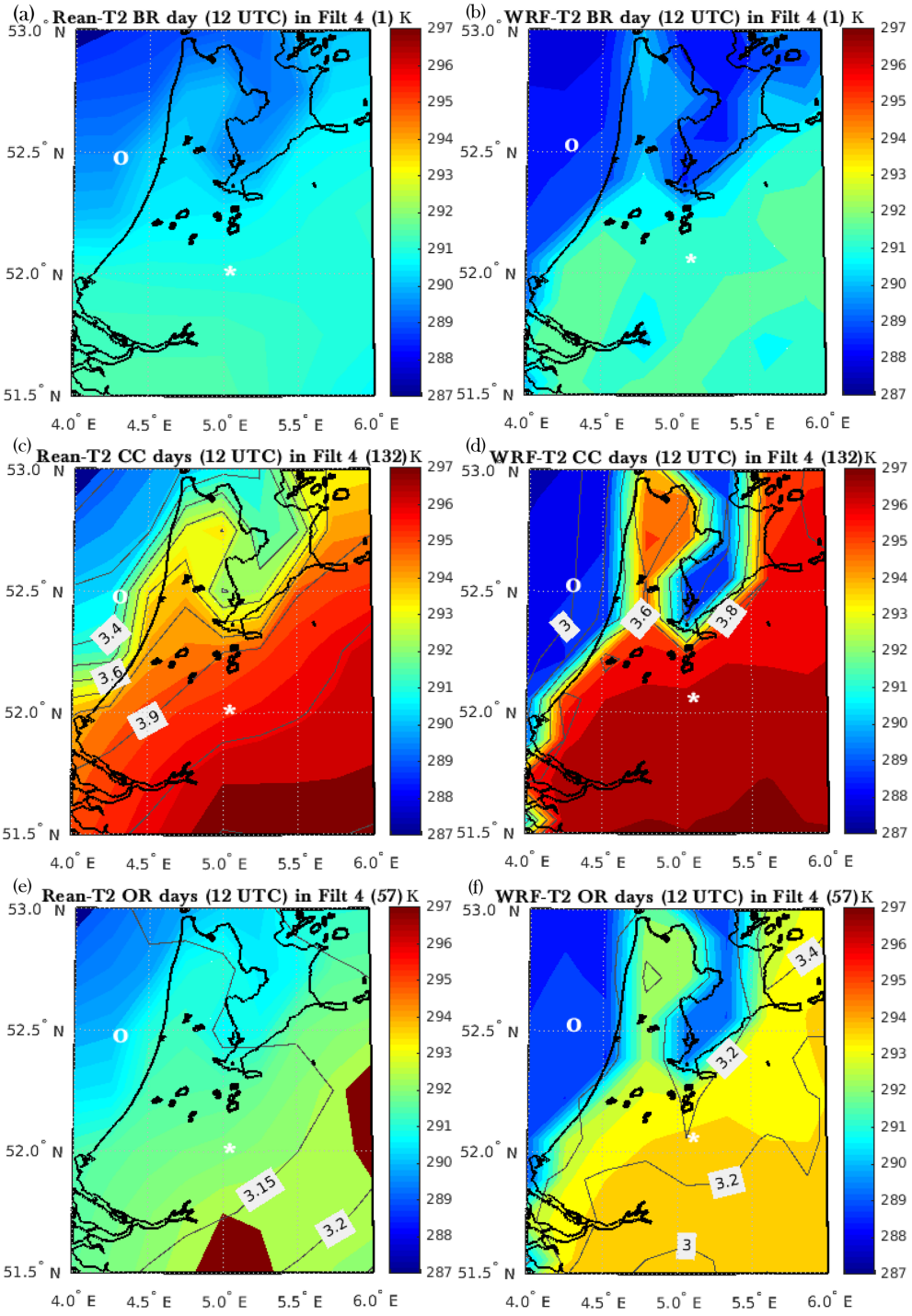

Figure 5. Composite maps of T at 2 m in the coastal area around Cabauw, from reanalysis data and WRF simulations, for different groups of events: both-rejected (BR), coincident (CC), and WRF-rejected (WR) days in Filter 4. The number of events of each group is included in brackets. The gray contours with the labels represent the standard deviation of the composites. The white circle pinpoints the grid point over the sea, and the white asterisk represents the grid point corresponding to Cabauw. Note that their position is slightly different in the model and in the reanalysis.

the observations but not by the WRF database until the third filter. The average observed precipitation is of (1.0 ± 0.6) mm in this case. Therefore, we can conclude that WRF overestimates remarkably the amount of days with low rainfall: 25 in which the recorded precipitation is below 0.1 mm, contrasting with the 4 from the observations. As a consequence, the number of selected SB days is reduced in WRF.

Filter 4 rejects days in which a minimum land-sea temperature difference of 2 K at 12 UTC is not exceeded. Figure 5 shows composites of the 2-m air temperature in the coastal area around Cabauw at that time, for the reanalysis and WRF simulations. This filter discards only one event in WRF, which is also rejected in the observations (BR day). The land-sea temperature contrast, measured from the difference between the grid point corresponding to Cabauw and the grid point over the North Sea, is almost null in the reanalysis (Figure 5a), whereas it is notably greater in the model (Figure 5b), although <2 K. The overestimation of the land-sea temperature gradient is more evident in the 132 CC days. The average ΔT is of ≃4 K in the reanalysis and ≃8 K in WRF. This great overestimation arises partially from slightly greater simulated temperature inland (∼1 K), but particularly from the significant lower simulated temperature over the sea (∼3 K). The 57 OR days also show this bias, reflecting the almost negligible effect of this filter in the numerical simulations. The slight overestimation of the temperature over land is partly driven by that of the SH flux over land, as will be shown later. Part of the bias could be driven by the LSM and the representation of the soil moisture, which exerts an important influence on the energy distribution between the turbulent fluxes. In any case, the physical processes taking place in the surface layer, particularly close to the land/sea-air boundaries, are in some cases not well captured by mesoscale models (e.g., Cuxart et al., 2015). Reproducing more realistic land-sea contrasts is therefore still a challenge.

On the other hand, it can be noted that the temperature decrease from the continent to the sea is graduated and smooth in the reanalysis, whereas it is very sharp and restricted to the coastal area in the WRF simulations. This difference arises partly from the higher horizontal resolution from WRF compared to the reanalysis and can also be connected with the thermal characteristics of the simulated SBFs. This and other physical aspects of the SBFs are compared and analyzed later in section 4.2.

3.3. Local Influences

The last filter evaluates the wind veering produced by the SBF passage. It selects days with a minimum veering or shift of 45° in the wind direction between 10 and 20 UTC, followed by a 2-hr period in which the onshore direction is maintained with a slight oscillation (in average below 15°) around this last direction. Days with a shift above 22.5° followed by an average oscillation below 5° are also accepted. Filter 5 turns out to be very selective when applied to the model and rejects around 73% of the days that pass Filter 4. Part of the rejection, however, arises from the adaptation of this filter from 10-min to 1-hr time resolution, as occurs in the observational database. In AR18, 102 SB events resulted from the application of the filter with 10-min resolution, 27 more than employing 1-hr resolution. Approximately half of the 27 rejected days are rejected due to a lack of a sufficiently large veering of the wind, while the rest are discarded due to excessive oscillation of the direction after the veering.

We analyze this filter by exploring the wind roses before (left) and after the onset (right) in Figure 6. In the former, the wind direction just before the onset is represented, together with the magnitude of the veering at the onset. In the latter, we show the wind direction at the moment of the onset and the average oscillation of the wind direction 2 hr after the onset. We compare the 10-m wind speed from the observations in Cabauw and from the grid point closest to Cabauw in the smallest domain of the WRF simulations. In this figure we do not analyze the days rejected by this filter, but the accepted ones. Apart from the CC days, the wind roses are shown for the WRF-accepted (WA) and observations-accepted (OA) days, which are accepted in each database but not in the other. The WA and OA days must not be confused with OR and WR days, respectively: Indeed, the WR days, for instance, are not necessarily OA days in each filter, since the second can have been rejected in WRF in any of the previous filters.

In the CC days the directions with a southerly component (90–270°) dominate in the observations before the onset (Figure 6a), whereas northerly directions (270–90°) dominate in the case of WRF (Figure 6b). This discrepancy can be explained by the great variability in the wind direction prior to the SB onset, coinciding with the wind-speed decrease, which is misrepresented in the models (such as for instance was found in Jiménez, Simó et al., 2016). As a consequence, the magnitude of the veering is greater in general in the observations. At the onset, SB directions are slightly shifted toward the NW and NE in the model (Figure 6h), underestimating the north SB frequency. The oscillation 2 hr after the onset is similar in both databases. In

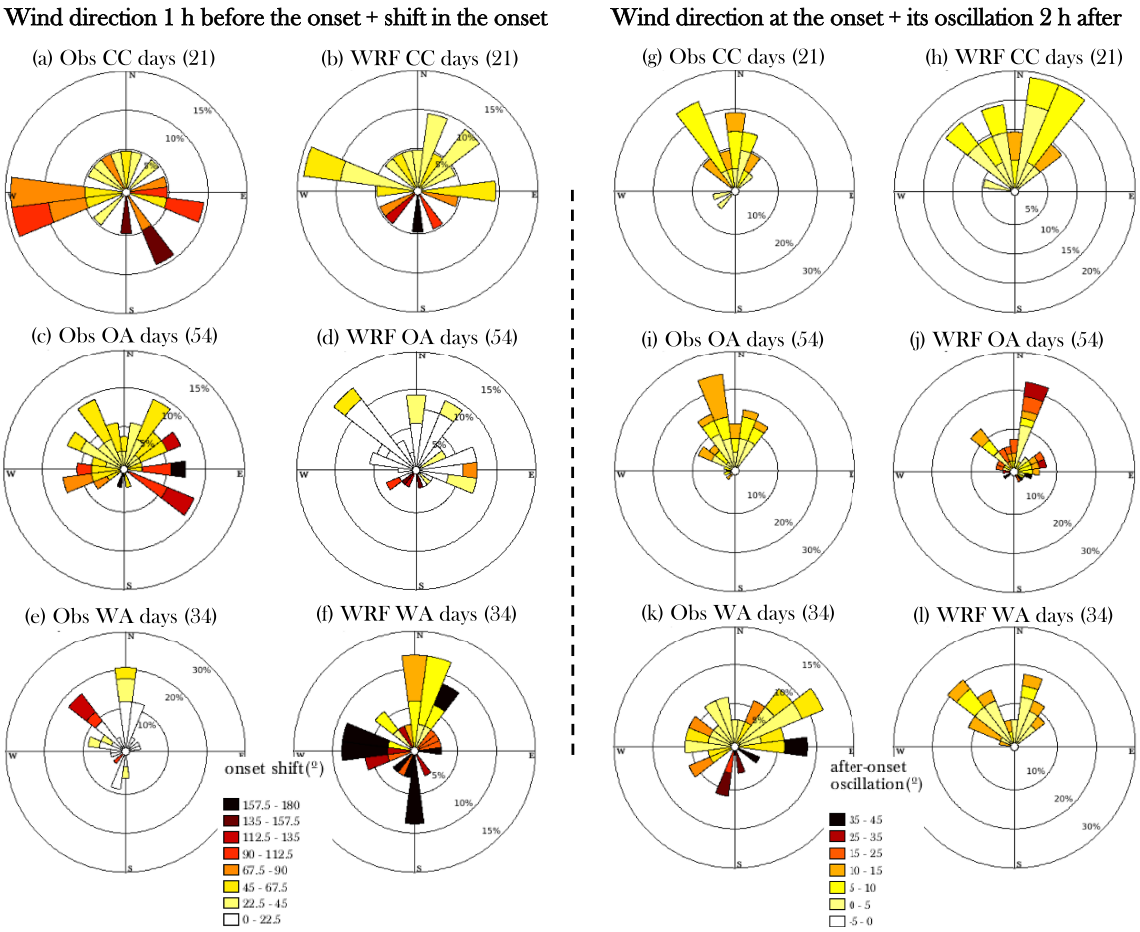

Figure 6. Wind roses at 10 m from reanalysis data and WRF simulations, for different groups of events: coincident (CC), observations-accepted (OA), and WRF-accepted (WA) days in Filter 5. The number of events of each group is included in brackets. To the left of the dashed vertical line, wind roses show wind direction 1 hr before the onset, and the colors show the magnitude of the veering in the onset, whereas to its right, they show the wind direction at the onset and the colors the average oscillation of the wind direction 2 hr after the onset.

the 54 OA days the wind direction before the onset is similar in the observations and WRF, but the veering of the wind is significantly smaller in WRF: it is just above 22.5° in few cases. Note that the onset reference employed in the WRF wind rose of the OA days is the same from the observations, and vice versa in the WA days. The observational wind direction at the onset is very similar from the CC days (Figure 6i). Except for few E-SE directions, the wind directions in WRF show SB directions, but with an excessively large oscillation after the onset in some cases. In any case, the change of the wind rose from before onset (Figure 6d) until the moment of the onset (Figure 6j) suggests that the model could be reproducing a SBF passage, although it does not meet the requirements from the algorithm in this filter. In the WA days the prevailing directions are north and NW (Figure 6e), indicating that the SB onset may already have occurred in the observations by the time WRF reproduces it, but it is not accepted by the requirements of the algorithm. A large part of the rejection in the observations occurs due to the great oscillation of the wind direction after the onset (Figure 6k). The evolution of the observational wind roses from before until the onset does not suggest the existence of a SB passage in this case, unlike the wind roses from WRF on the OA days.

It is noteworthy that there are more OA than WA days in Filter 5 (54 vs. 34). It must be emphasized that this does not necessarily imply that WRF reproduces fewer SB days but that the frontal requirements from the algorithm are more frequently met in the observations than in the WRF database. In fact, the application of the algorithm is not carried out to obtain statistics of SB occurrences in Cabauw but to select clear SBF passages. One relevant question regarding our scaling analysis is in which filters are the 54 OA days discarded in the WRF database: 20% in Filter 1, 15% in Filter 2, 17% in Filter 3, none in Filter 4, and 48% in Filter 5.

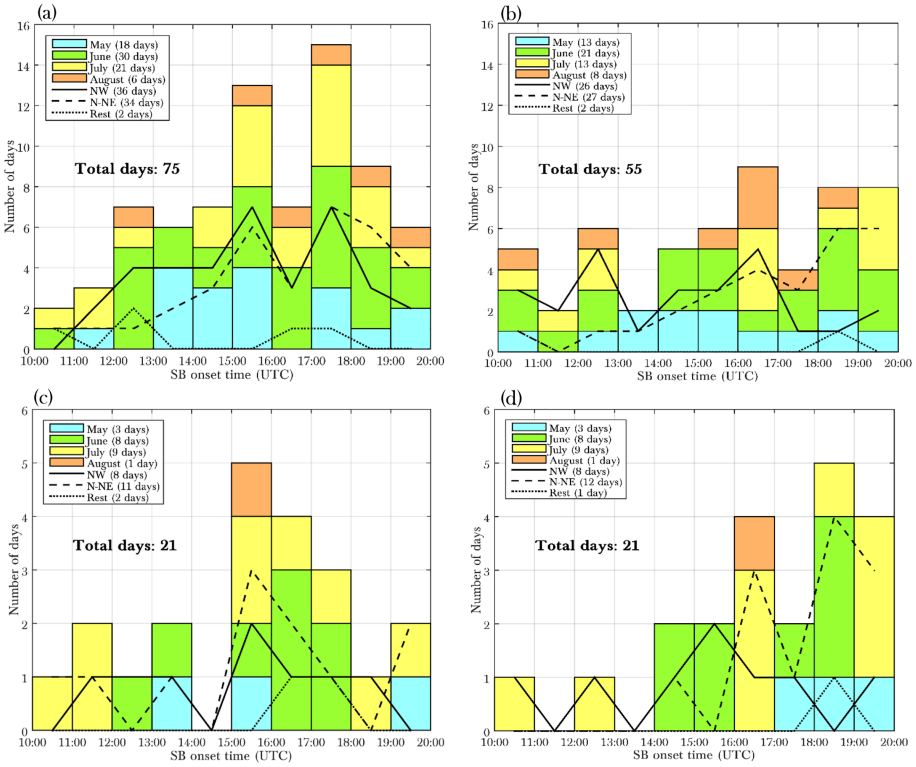

Figure 7. Histogram of onset times for the (a) 75 observed, (b) 55 simulated, (c) 21 coincident days in the observations, and (d) 21 coincident days in WRF. The monthly distribution is shown in colors, and the wind-direction distribution in black lines. The frequency scale (*y* axis) is the same between (a) and (b), and (c) and (d). Local summer time is UTC + 2.

The greatest discrepancy results clearly from Filter 5, which is very demanding to assure that the final days are clear SBF passages.

The resultant 21 CC events are the ones employed to carry out the verification of the model, as well as the analysis of the reproduced SBF characteristics and their interaction with turbulence in section 4. From the 21 CC days, 18 are within the 102 resultant events previously discussed by AR18. Hence, the 21 CC SB days may not be absolutely representative of the observed SB characteristics in Cabauw (as from AR18) but allow an objective and consistent comparison with the SB events reproduced by the WRF model.

4. Assessment of the Model Performance

Before fully focusing on the analysis of the 21 CC days, these are compared with the 75 and 55 selected SB days from the observational and WRF databases (see last line from Table 2) in the following subsection.

4.1. SB Databases

We start contrasting the SB databases from the observations and WRF by clustering them together in histograms (Figure 7). They illustrate the frequency of SB onset at different times of day, shown for different months and SB directions (NW and N-NE). As was concluded in AR18, the synoptic horizontal pressure gradient is mainly responsible for the different SB directions. The NW SB [290–350°], which is formed in the North Sea (see Figure 1), develops under a high-pressure system to the south of the Netherlands, whereas the N-NE [350–45°] SB is propagated over the Markermeer and IJsselmeer closed seas (see Figure 1) when the high-pressure system is to the north of the country.

Comparing first the 75 observed (Figure 7a) and the 55 simulated (Figure 7b) SB events, we find that WRF does not reproduce the increase in the onset frequency between 1500 and 1900 UTC as in the observed SB days. That increase was even more clearly observed from the 102 SB days in AR18. The absence of the increase in the simulations is directly linked with the fact that mesoscale models misrepresent the acceleration in the inland propagation of SBFs in the late afternoon, when convection is already decaying

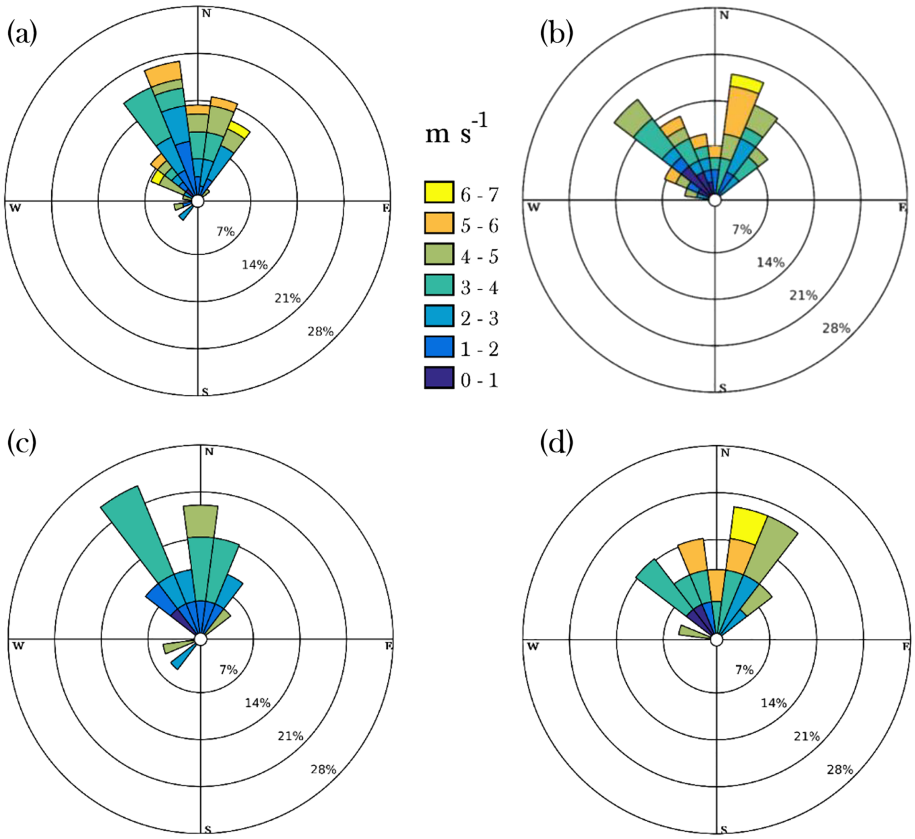

Figure 8. Ten-meter wind roses at the SB onset for the (a) 75 observed SB days, (b) 55 simulated SB days, (c) 21 coincident days from observations, and (d) 21 coincident days from WRF.

(Crosman & Horel, 2010). Hence, the distribution of SB-onset frequencies is more uniform throughout the day in the model. The wind-direction distribution is different as well. We find an increase in the frequency of NE SBs and a decrease of the NW SB days at the end of the day particularly for the SB events from WRF. As can be noted from Figure 1 the area surrounding Cabauw is very flat, so that the influence of topography in the SB direction is null. Hence, we can hypothesize that WRF overestimates the relative weight of the Coriolis term and advances its influence in the late afternoon/evening, which would explain the greater and earlier increase of the NE SB directions. More light is shed into this issue later in subsection 4.3, when comparing the daily wind evolution for two individual cases.

Regarding the 21 CC days (Figures 7c and 7d), the maximum in the onset frequency is delayed in the model: It is observed between 1500 and 1800 UTC, but in the model takes place roughly between 1600 and 2000 UTC, clearly contrasting with the uniformity of the distribution from the 55 simulated days (Figure 7b). From individual inspection of the CC days (not shown), we find that the onset time of SBs is overall delayed in the model: The onset-time bias is around 25 min. Furthermore, the delay or advance in few individual events is even greater than 5 hr. We calculate a RMSE of the onset time of almost 4 hr, indicating that the model has an important deviation in reproducing the exact onset time of the SB passage as it is defined in the algorithm. However, the bias is in a large part affected by the difficulty of capturing the frontal passage from the last filter. Salvador et al. (2016) also reported a delay of the WRF model in reproducing the SB onset, associated with the opposing effect of the offshore synoptic wind. The lack of coincidence in the SB onset times can also be noticed from the monthly distribution of the histograms. The increase of NE SBs between 1600 and 2000 UTC is also evident in the 21 CC days from WRF.

We further explore the performance of the model in reproducing the observed SB direction and intensity from wind roses at 10 m agl in Figure 8. As stated before for the CC days from Figure 6, the model tends to shift the SB directions toward the NE and NW (Figure 8b), underestimating the north SB frequency from the observations (Figure 8a). It has to be taken into account that the model at 2-km resolution may not

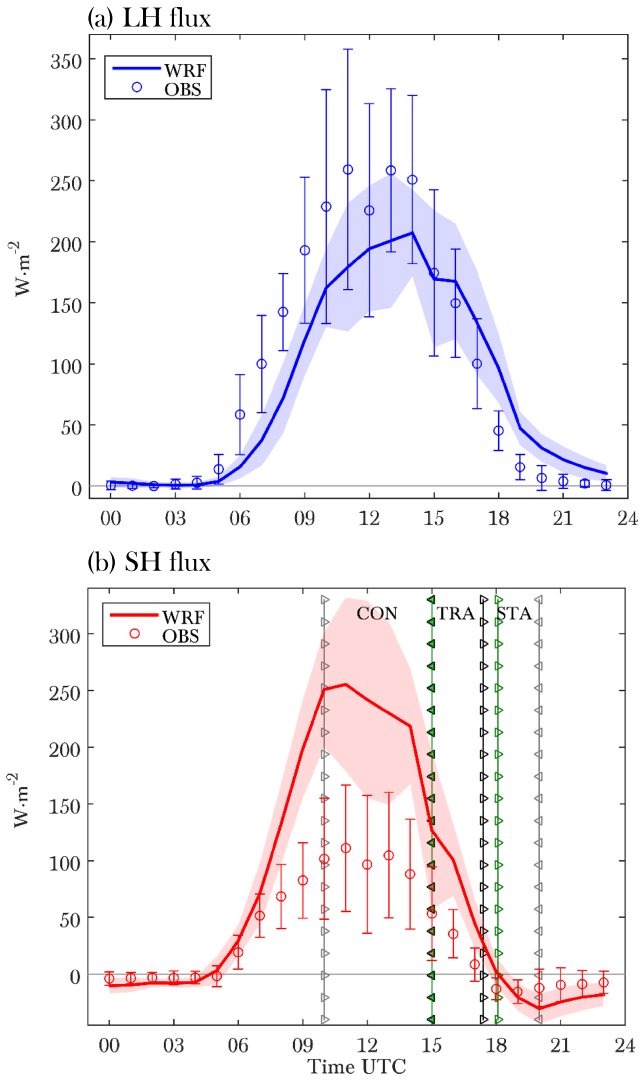

Figure 9. Time evolution of the average (a) latent-heat and (b) sensible-heat fluxes and their standard deviation on the 21 coincident SB days, in circles for the observations and solid lines for the numerical simulations. Vertical lines with triangle markers in (b) delimit the sensible-heat flux values for the 3 ABL regimes (convective, transition, and stable), in green for the model, and in black for the observations. Gray vertical lines are coincident for the model and the observations.

adequately include the more local scales. On the other hand, the 21 CC observed SB events are clearly weaker than the 75 observed days. Comparing the 55 simulated days (Figure 8b) with the 21 CC simulated days (Figure 8d), we find a decrease of the NW SB cases (again the most intense ones). On the other hand, comparing the numerical simulations and observations on the 21 CC days, we find that WRF overestimates slightly the SB intensity, especially in the case of NNE SBs. The enhancement of the NNE SB intensity can be linked with the fact that WRF tends to sharpen the thermal gradient between the Markermeer and IJsselmeer closed seas and Cabauw, comparing with the gradient between the North Sea and Cabauw (see Figures 5c and 5d). In addition, the systematic and positive bias in the wind speed that is usually present in WRF (in average of 0.4 m/s as calculated in Jiménez, Simó et al., 2016) also contributes to the stronger SB intensity. Besides, we conclude that the strongest SB events from the observations are not selected by WRF and the intensity of some of the selected ones is overestimated. This latter finding contrasts with the conclusions from Hughes and Veron (2018), where they found weaker SBs which dissipate earlier in the model.

4.2. Interaction With Local Turbulence

In the previous subsection, we have compared the onset features of all the SB days selected by the algorithm both from the observations and WRF simulations. However, as discussed in AR18, the SBF arrives in Cabauw

in most of the cases during AET of the ABL, a stage in which a complex decay of turbulence takes place (Lothon et al., 2014). Hence, the local-turbulence and stability conditions at the arrival time of the SBF are fundamental to understand the subsequent evolution of the SB and its impact on the lower atmosphere.

4.2.1. ABL Regimes

From the value of the SH flux at the onset with respect to the diurnal maximum value, a classification of the SB events into three ABL regimes is carried out: convective, transition, and stable regimes (for further information we refer the reader to section 4 in AR18). To show the differences in local forcings, we compare the latent heat (LH) and SH fluxes in Figure 9. In the case of the latter, those differences have an impact on the regime classification.

WRF overestimates around 20% the peak value of the LH flux and delays its evolution about 1.5 hr (Figure 9a) on the SB days. The overestimation of the SH flux is significantly greater (more than 100% for the peak), whereas the delay in the evolution is smaller than for the LH flux (Figure 9b). By comparing the standard deviation of observations and simulations, we find that during daytime, in spite of having a wide range of variability, the evolutions of the SH do not overlap. Regarding the rest of the terms of the surface-energy balance (not shown here), the net radiation is slightly overestimated in the model during daytime (up to 15–20%), whereas the soil-heat flux is adequately represented. The latter is calculated in an explicit way as the residual flux of the net radiation and the turbulent fluxes. The methodology and corrections employed to calculate the observational soil-heat flux are detailed in Ronda and Bosveld (2009).

Hence, there is a slight excess of the available energy reaching the surface in the model. Previous sensitivity experiments carried out with our numerical database have shown that the overestimation of the SH flux could be offset by employing lower and more realistic values of the albedo and by enhancing the soil-moisture values (not shown). Moreover, this strong overestimation of the SH flux was also observed in the simulations carried out in the area of Cabauw from the WRF model in Steeneveld et al. (2011), although the temperature profiles were adequately reproduced. Sun et al. (2017) found an overestimation of the SH flux of similar magnitude using the YSU ABL scheme in their simulations from the WRF model, but in this case producing a positive bias in the 2-m air temperature. On the other hand, it must also be taken into account that measurements tend to underestimate the turbulent fluxes as reported for instance in Foken (2008). Also related, the surface-energy imbalance in Cabauw, as in other sites around the world, is a well-documented issue (e.g., Bosveld, 2010; de Roode et al., 2010).

On the other hand, the model delays approximately 1 hr the moment at which the SH reverses it sign. Even though the delay is more evident in the case of the LH flux, it is more relevant in the case of the SH flux, since it is one of the main drivers in establishing the unstable or stable stratification around Cabauw. By way of example, the stable regime is established almost 1 hr later in the model, and hence, the SBF arriving in the simulation at the same time as in the observations evolves dynamically in a different way. This can be an important source of bias when forecasting SB phenomena and the variables closely related to them. Hence, a better representation of surface and ABL processes is highly relevant in a mesoscale model.

We compare in Figure 10 the average wind speed, potential temperature, specific humidity, and MLH for the model and observations on the 21 CC SB days by classifying them into the three ABL regimes. The average for each regime was calculated by normalizing all the events with respect to the SB onset. The simulated variables in this figure are taken from the gridpoint closest to Cabauw.

First, from the 21 CC days we find that 5 (5 in WRF) are within the convective regime, 12 (10 in WRF) in the transition regime, and 4 (6 in WRF) in the stable regime. However, it is remarkable that we only find regime coincidence in 1/5 of the cases from the convective regime, 6/12 from the transition regime, and 1/4 from the stable regime, which makes the comparison more challenging. In any case, the conditions for each regime are similar in terms of local turbulence, and therefore, the comparison is yet consistent. Besides, due to the quality control of the MLH estimation from the wind profiler, 61% of data were missing, and therefore, we just represent the simulated values coinciding with observed MLH data.

In general, the impact of the SBF on the represented variables is different depending on the ABL regime, and WRF simulations differ in how this impact is manifested. At this point it is necessary to note that the reader can find a lack of similarity with the results presented in AR18. That is due to two main reasons: First, the time resolution in this study has been adapted to 1 hr, so that the evolution of the different variables is smoothed, and second, we only show 21 events (from which 18 are coincident with the 102 employed in AR18).

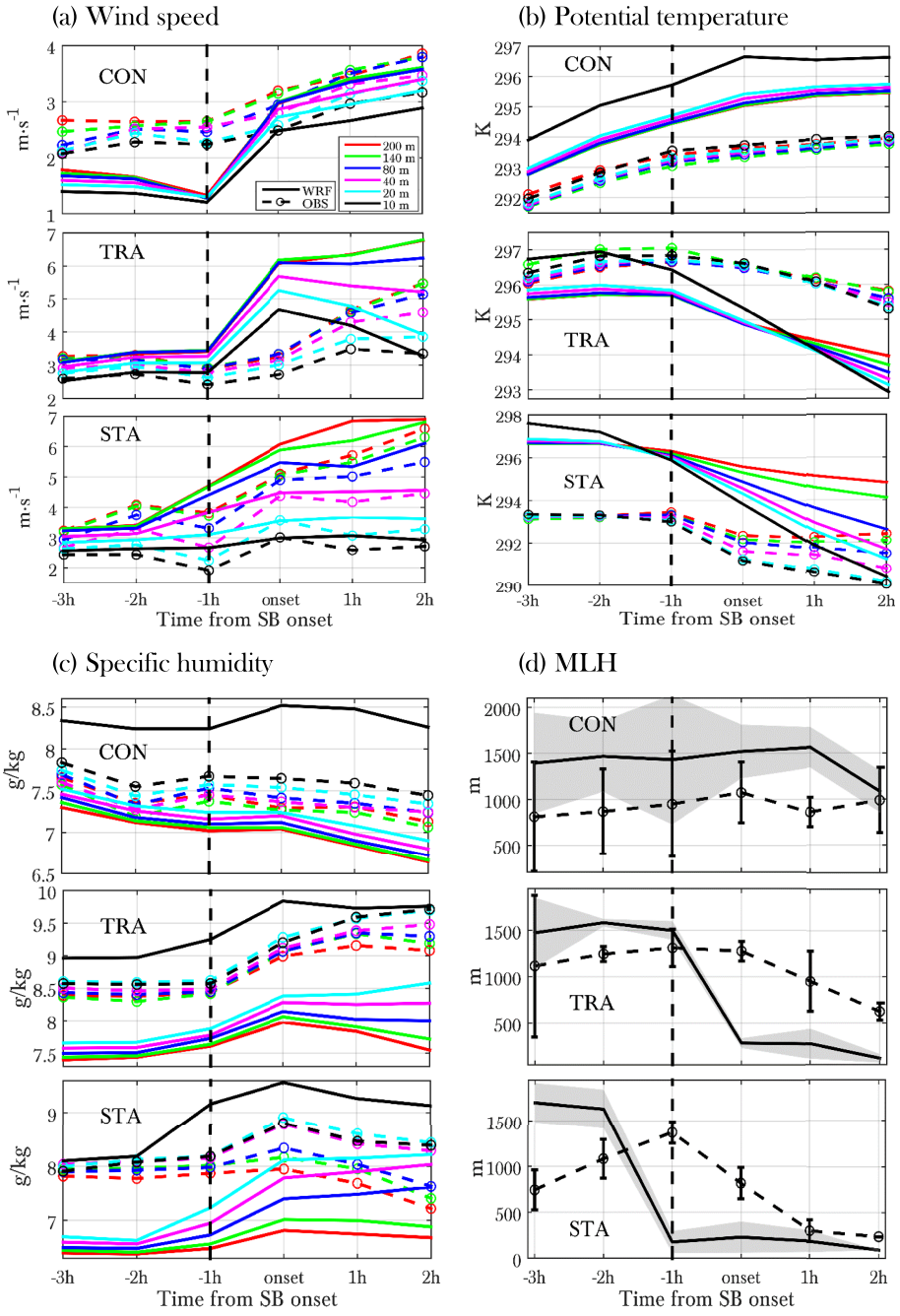

Figure 10. Time evolution of the average (a) wind speed, (b) potential temperature, (c) specific humidity, and (d) MLH and its standard deviation between 3 hr before and 2 hr after the onset of the 21 coincident SB days for the three ABL regimes (convective, transition, and stable). The dashed vertical line identifies the 1-hr measurement just before the onset, which occurs between the dashed line and time = 0.

Starting with the convective regime, wind speed is underestimated by around 1 m/s prior to the SB onset (Figure 10a). The reproduced SBF in the model is sharper, which is in agreement with the stronger SB intensity observed in Figure 8d. Potential temperature is considerably overestimated (up to 2 K after the onset) and specific humidity underestimated (around 0.5 g/kg). The simulated specific humidity at 10 m is considerably biased with respect to the rest of the levels and also with respect to the observed values, which is illustrating a remarkable bias from the WRF model in computing this variable near the surface. With respect to the MLH, it is approximately between 400 and 700 m deeper in WRF, which could be partly influenced by the issue of the wind profiler in detecting the top of the mixing layer. In any case, the above commented

biases in the model for the potential temperature, specific humidity, and MLH can be explained by the great overestimation of the SH flux. A greater SH flux induces a greater warming of the lower atmosphere, greater convection, and a stronger vertical mixing with drier air above. Regarding the intensity of SBFs, the enhanced SH flux has an opposite effect. On the one hand, the induced greater convection reduces the intensity of SBFs by producing frontolysis, that is, by increasing the mixing between the maritime and continental air masses (Ogawa et al., 2003). On the other hand, the greater SH flux over land sharpens the land-sea thermal contrast and consequently increases the inland penetration and intensity of the SBF (Crosman & Horel, 2010). Since in our case the modeled SBFs are stronger, it seems that the second effect with a more mesoscale character dominates over the first.

In the transition regime both the SBF intensity and the stratification of the wind speed 2 hr after the onset are slightly overestimated. The four variables show a sharper transition in the model, from well-mixed conditions 3 hr before the onset to an already stratified lower atmosphere 2 hr after the onset. For instance, the vertical difference between 20 and 200 m for the specific humidity is of ∼0.2 g/kg 3 hr before the onset both in observations and WRF, and of ∼0.6 g/kg in the observations and ∼1.1 g/kg in the numerical simulations 2 hr after the onset. The acceleration of the afternoon transition (AT) due to the SBF passage observed in AR18 is overstated in WRF. In the model the transition from convective to stable depends on the value of the Richardson number and for that reason takes place abruptly, which could also contribute to the acceleration of the AT.

In the stable regime the stratification is already stable when the SBF arrives, but as it occurs in the transition regime, the stabilization process is enhanced in the model. We quantify this effect by analyzing the evolution of the potential temperature and the specific humidity. In the case of the former variable, for instance, the vertical difference between 10 and 200 m is of around 1 K 3 hr before the onset in the observations and of 0 K in WRF, whereas it reaches −4.5 K in the observations and −2.5 K in the model 2 hr after the onset. The MLH shows a contrasting behavior in the model. Before the arrival of the SBF the observed MLH shows a peak (∼1,300–1,400 m) despite the SH flux turns negative, whereas the model reproduces a shallow MLH, typical of the nocturnal regime (∼200 m). As above commented, this difference can be partly associated with the issue from the wind profiler itself (de Haij et al., 2007), which could be detecting the top of the residual layer during the evening transition (ET). On the other hand, the MLH is determined from different criteria in the observations and numerical simulations, which also increases the discrepancy. Likewise, the parameterizations of the surface layer are based on Monin-Obukhov Similarity Theory (MOST) formulation. As was concluded in AR18, MOST fails in reproducing the surface-layer wind profile just after the SB onset, which could also explain the considerable bias.

4.2.2. Impact on Turbulence

In order to quantify the impact of the SB passage on local turbulence during the AET of the ABL, we investigate the evolution of the friction velocity (u_*) related with mechanical turbulence, and convective velocity (w_*) related with thermal turbulence, for the three ABL regimes (the second just in the convective regime) in Figure 11. The calculated observational u_* considers a regional wind-direction dependent roughness length. In this way, the comparison with grid u_* from WRF is more optimal and less dependent on the local conditions around the 213-m tower in Cabauw (Beljaars & Bosveld, 1997; Verkaik & Holtslag, 2007). The observational w_* is calculated as the free-convection scaling velocity (Deardorff, 1972):

$$w_{*,obs} = \left(\frac{g}{\theta_v} \overline{w'\theta'_v} Z_i \right)^{1/3}, \tag{1}$$

where θ_v is the virtual potential temperature at 2 m, $\overline{w'\theta'_v}$ is the upward kinematic heat flux, and in Z_i we replace the MLH from the wind profiler. w_* is only defined when $\overline{w'\theta'_v} > 0$, and since that requirement is only assured between 2 hr before and 2 hr after the onset in the convective regime, it is just calculated for this ABL regime.

Since we lack the upward kinematic heat flux in the model output, we calculate w_* from the definition of the SH flux:

$$w_{*,mod} = \left(\frac{g}{\theta_v} \frac{H}{\rho c_{pd}} Z_i \right)^{1/3}, \tag{2}$$

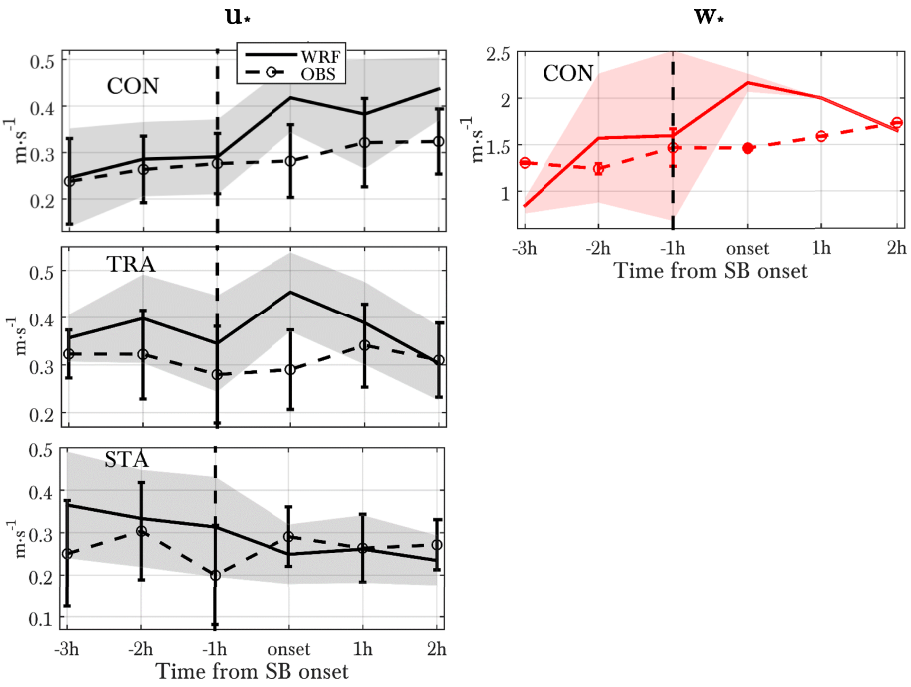

Figure 11. Time evolution of the average friction velocity (in black, left), convective velocity (in red, right), and their standard deviation between 3 hr before and 2 hr after the onset of SBs for the 21 coincident SB days, separated in the three ABL regimes (convective, transition, and stable). The dashed vertical line identifies the 1-hr measurement just before the onset, which occurs between the dashed line and time = 0.

being H the SH flux (W/m^2), ρ the air density at 2 m, and c_{pd} the specific heat of the dry air at constant pressure. We substitute in this case the modeled MLH in Z_i, which is calculated from the critical Richardson number.

In the convective regime the enhancement in u_* associated with the passage of the SBF is overestimated, which is in agreement with greater modeled wind-speed increase. However, the enhanced vertical mixing in the model compensates the underestimation of the wind prior to the SB onset (see Figure 10a), and hence, the values of u_* are similar before the arrival of the SBF. The values of w_* in the model represent a significant increase at the SB onset (above 1.3 m/s from 3 hr before), contrasting with the observations (it roughly increases 0.2 m/s in 3 hr). This overestimation is influenced by the greater vertical mixing (evident from the comparison between the SH flux and the MLH), and in particular from the increase of the SH flux in the model. In any case, the simulated quantity carries out a significantly greater variability than in the observations (note the difference in the standard deviation). In the transition regime u_* is overestimated around 50% at the moment of the onset. In AR18 they proved how the increase of the shear induced by the SBF resulted in an acceleration of the AT, so that the stable stratification was established before. The increase of mechanical turbulence is greater in the model, which explains the sharper AT taking place in the numerical simulations (see Figure 10). However, the overestimation of local turbulence after the SB onset is not present in the stable regime, and the simulated u_* follows the observed one. In any case, the different variables represented in Figure 10 indicate that the lower atmosphere evolves in a distinct way once the stable conditions are achieved. As reported in AR18, in the stable regime the onset of the SB brings the wind profile within the surface layer out of the equilibrium with local turbulence. Since the ABL parameterizations in WRF are based on MOST formulation, discrepancies can be expected in the evolution of distinct atmospheric variables during the ET when the SBF arrives within this stage.

4.3. Individual Case Studies

Two individual representative case studies are shown in Figure 12 to complete the analysis, comparing the daily evolution of the wind vectors. The 850-hPa wind from both the reanalysis and WRF simulations for those events at 6, 12, and 18 UTC is also included to represent its influence. One of the case studies (27 July 2002) represents a CC event in which the 850-hPa wind is very similar between the model and the reanalysis,

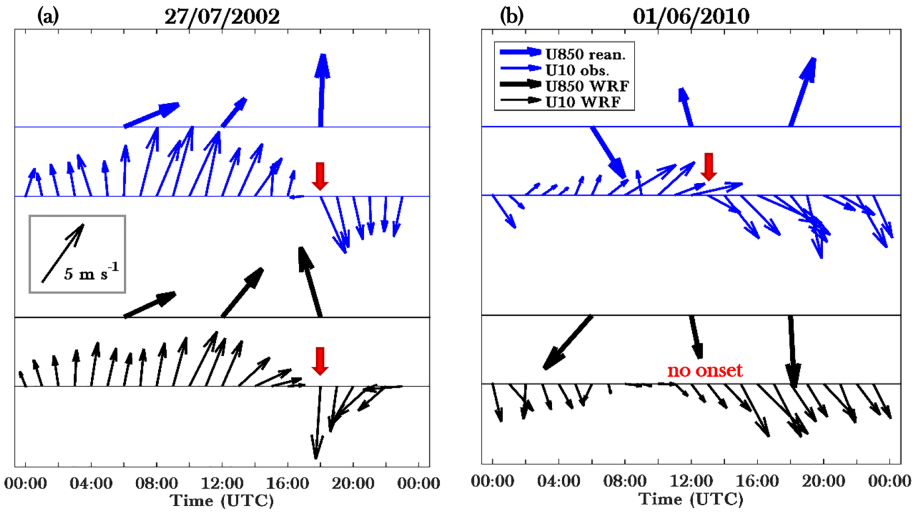

Figure 12. Daily evolution of the wind vectors in two case studies. For each event, the evolution of the 10-m and 850-hPa wind vectors (the latter is shown at 6, 12, and 18 UTC from thicker arrows) is represented for the observations (blue) and numerical simulations (black). The corresponding SB onset is pointed by red arrows.

and the SB onset takes place simultaneously. The other event is an OA + WR day from Filter 5 (01 June 2010), in which the 850-hPa wind is notably biased compared with the reanalysis and so is the wind-vector evolution at 10 m.

On the event corresponding to the 27 July 2002 the wind veers from the SSW to the NNW at 1800 UTC (in blue, Figure 12a), which is identified by the last filter of the algorithm as the passage of the SBF. The wind direction prior to the onset is almost parallel to the large-scale wind. In fact, in the absence of influencing topographical features, and before the onset of the SB, the wind direction in Cabauw is mainly ruled by the large-scale wind. Under very similar large-scale conditions, the model (in black) reproduces closely the wind direction and intensity before and after the SB onset. The only slight discrepancy is that the wind after the SBF passage blows from the NNE instead of NNW, partly influenced by the large-scale wind, which blows from the SSE instead of south as in the reanalysis. Besides, as commented before, the thermal gradient between the IJsselmeer and Cabauw is enhanced in the model, intensifying the NE SBs. And additionally, in the observed SB days generally from 20 UTC on, the wind veers toward the ENE as a general trend (not shown) influenced by the Coriolis force when the mesoscale gradient is weakened, as has also been reported in previous observational and numerical analyses (Miller et al., 2003; Steele et al., 2013). The veering toward the ENE is in many cases advanced and sharpened in the model, as can also be evidenced from Figure 12a and Figures 7b and 7d. This suggests that the relative weight of the Coriolis term in the momentum budget is overestimated in the model during the ET.

The bias in the large-scale wind is clearly manifested in the different wind-vector evolution on the 1 June 2010 (Figure 12b). In the reanalysis, the wind at 850 hPa blows from the south component at 12 and 18 UTC, and the observed SBF passage produces a veering of the wind from the SW to NW at 13 UTC. In the model, however, the wind at 850 hPa is largely biased and blows from the north component at 12 and 18 UTC. As a consequence, the wind blows from the NW throughout the day, and the SBF passage is unrecognizable from the wind direction, if existed that SBF in the model.

This result has evidenced the relevance of adequately simulating the large-scale conditions for a better SB forecasting. As has been reflected, the wind-direction veering is not only affected by local features, but also in an important manner by the synoptic wind even in days not dominated by the synoptic conditions, since those events are rejected in the first two filters of the algorithm.

5. Conclusions and Future Prospects

SB frontal passages from a 10-year observational database, and from WRF numerical simulations spanning the same period, have been compared and analyzed in this study. The methodology employed follows Arrillaga et al. (2018), in which the research strategy was applied solely to the observational database. This

study extends the analysis to the numerical simulations. To select the SB events, a systematic algorithm based on objective criteria is applied with the same thresholds to the variables from both the observations and numerical simulations. One of the focuses has been put on disentangling the role of the large scale, mesoscale, and local factors giving rise to discrepancy in the objective and systematic SB detection employed. Below, we summarize the most relevant findings grouped according to the role of the different scales:

1. Synoptic scales: Around 30% of the discrepancy in the SB selection between the observations and numerical simulations arises from biases in the large-scale conditions. The simulated synoptic wind at 850 hPa, in terms of intensity and direction, shows a satisfactory correspondence with the reanalysis. However, local unrealistic representation of the synoptic wind, with an average bias of up to ± 2 m/s in Cabauw, gives rise to discordance in few cases. In connection with the rejection of cold synoptic fronts, composite maps of the equivalent potential temperature show that the decrease in this variable is slightly overestimated in the model. Hence, the number of cold synoptic fronts is overstated, leading to a decrease in the final number of SB days.
2. Mesoscales: The smallest discrepancy in SB events coincidence (6%) comes from mesoscale forcings. With respect to exclusion due to precipitation, rejection is greater in the model (28% vs. 18%), particularly due to the amount of days with low rainfall. Regarding the land-sea temperature gradient, the filtering of days with small gradient is almost negligible in WRF, as a result of the great overestimation in this magnitude, of up to 4 K in average. The enlarged gradient originates to a larger extent from the important underestimation of the air temperature over the sea, and to a lesser extent from higher inland temperature, associated with the overestimation of the SH flux.
3. Local scales: The last filter from the algorithm is linked with the SB frontal passage, evaluated from the evolution of the local surface wind direction. The strict requirements from this filter produce the greatest rejection of days, particularly in the model database. In some rejected events in the observations and in the model, the wind roses show the possible presence of the SB but are not finally selected objectively as SB days due to a lack of a sufficiently large wind veering or due to excessive oscillation after the veering. After applying this last filter, 21 SB days selected from the observational database are coincident in WRF. The onset time is considerably biased in some of the coincident events, which can in any case be linked with the challenge of capturing the frontal passage from an objective filter.

The simulated SB characteristics in the 21 coincident days show in general a good correspondence with the observed ones, but some discrepancies are also revealed. First, the SB intensity is slightly overstated in WRF, influenced by the enlarged land-sea thermal gradient and the systematic bias in the wind speed. On the other hand, we find a disagreement in the temporal distribution of SB directions. The veering from NW to NE directions occurs systematically earlier in the model. As inferred from the surface wind-vector evolution in two representative events, differences in the large-scale wind direction induce important alterations in the 10-m wind. However, since the large-scale wind does not show a systematic bias, we attribute the early veering to an overestimation in the relative weight of the Coriolis term in the model.

Finally, given the importance of the SB-turbulence interaction during the AET, as was proved in Arrillaga et al. (2018), the coincident SB events have been classified into different ABL regimes. These, are defined according to the local turbulence at the moment of the onset. The evolution of the different variables within the lower atmosphere reveals interesting results for the model. The acceleration of the afternoon transition as a result of the SBF passage is overstated. The stabilization process during the evening transition after the SB onset also occurs faster in WRF, which is evidenced from the rapid increase in the stratification of variables such as the specific humidity and the abrupt decrease in the MLH. Additionally, as a consequence of the stronger SBF passage, the values of the friction and convective velocity after the onset are significantly magnified by the model in the convective and transition regimes. Given the important influence of local turbulence in the characteristics of the SB, improving the representation of the AET in the model is necessary for getting a more realistic representation of the SB and its impacts.

The presented results can be considered a benchmark of the aspects to be improved in order to produce finer SB forecasts and more adequate representations of the associated physical processes, particularly during the AET of the ABL. The analysis has been carried out for one site but could be extended in future investigations by using more emplacements to explore the propagation of frontal passages and validate modeled spatial patterns.

Acknowledgments
This work was funded by the Projects CGL2015-65627-C3-3-R (MINECO/FEDER) and CGL2016-81828-REDT/AEI from the Spanish Government. Jon A. Arrillaga developed part of the research during a visit to Wageningen University, supported by a EGONLABUR mobility grant from the Basque government (EP_2016_1_0048). This material is based upon work supported by the National Center for Atmospheric Research, which is a major facility sponsored by the National Science Foundation under Cooperative Agreement No. 1852977. We thank the Royal Netherlands Meteorological Institute (KNMI) for the meteorological data from Cabauw, and we are particularly thankful to Fred Bosveld and Henk Klein Baltink for their collaboration on the observational data. We also thank Jimy Dudhia for his assistance in the performance of the WRF simulations. Observational data collected at the CESAR site can be obtained from the Cesar Database webportal (www.cesar-database.nl/). The variables from the numerical simulations employed in this study can be downloaded online (via the following link: https://eprints.ucm.es/58557/).

References

Ahmadov, R., Gerbig, C., Kretschmer, R., Koerner, S., Neininger, B., Dolman, A. J., & Sarrat, C. (2007). Mesoscale covariance of transport and co2 fluxes: Evidence from observations and simulations using the wrf-vprm coupled atmosphere-biosphere model. *Journal of Geophysical Research*, *112*, D22107. https://doi.org/10.1029/2007JD008552

Archer, C. L., Colle, B., Monache, L., Dvorak, M., Lundquist, J., Bailey, B., et al. (2014). Meteorology for coastal/offshore wind energy in the United States: Recommendations and research needs for the next 10 years. *Bulletin of the American Meteorological Society*, *13*, 515–519.

Arrillaga, J. A., Vilà-Guerau de Arellano, J., Bosveld, F., Baltink, H. K., Yagüe, C., Sastre, M., & Román-Cascón, C. (2018). Impacts of afternoon and evening sea-breeze fronts on local turbulence, and on CO2 and radon-222 transport. *Quarterly Journal of the Royal Meteorological Society*, *144*, 990–1011. https://doi.org/10.1002/qj.3252

Arrillaga, J. A., Yagüe, C., Sastre, M., & Román-Cascón, C. (2016). A characterisation of sea-breeze events in the eastern Cantabrian Coast (Spain) from observational data and WRF simulations. *Atmospheric Research*, *181*, 265–280. https://doi.org/10.1016/j.atmosres.2016.06.021

Azorín-Molina, C., Tijm, S., Ebert, E. E., Vicente-Serrano, S. M., & Estrela, M. J. (2014). Sea breeze thunderstorms in the eastern Iberian Peninsula. Neighborhood verification of Hirlam and Harmonie precipitacion forecasts. *Atmospheric Research*, *139*, 101–115.

Beljaars, AntonC. M., & Bosveld, F. C. (1997). Cabauw data for the validation of land surface parameterization schemes. *Journal of Climate*, *10*(6), 1172–1193. https://doi.org/10.1175/1520-0442(1997)010<1172:CDFTVO>2.0.CO;2

Borge, R., Alexandrov, V., José del Vas, J., Lumbreras, J., & Rodríguez, E. (2008). A comprehensive sensitivity analysis of the WRF model for air quality applications over the Iberian Peninsula. *Atmospheric Environment*, *42*, 8560–8574.

Borne, K., Chen, D., & Nunez, M. (1998). A method for finding sea breeze days under stable synoptic conditions and its application to the Swedish west coast. *International Journal of Climatology*, *18*(8), 901–914. https://doi.org/10.1002/(SICI)1097-0088(19980630)18:8<901::AID-JOC295>3.0.CO;2-F

Bosveld, F. (2010). Observering the surface energy budget at Cabauw: A status report (*Triennial Scientific Report No. 15-20*): Koninklijk Nederlands Meteorologish Instituut. Retrieved from https://pdfs.semanticscholar.org/139d/f5a98d35093eff99ec48d02d53a5036fd29f.pdf?ga=2.54337323.225448863.1574716374-1029577606.1574716374

Bosveld, F. (2017). Dataset-description document of the datasets in the cesardatabase (*Tech. Rep.*): KNMI. Retrieved from http://projects.knmi.nl/cabauw/insitu/observations/documentation/CabauwTR/CabauwTR.pdf

Bughici, T., Lazarovitch, N., Fredj, E., & Tas, E. (2019). Evaluation and bias correction in WRF model forecasting of precipitation and potential evapotranspiration. *Journal of Hydrometeorology*, *20*(5), 965–983. https://doi.org/10.1175/JHM-D-18-0160.1

Challa, V. S., Indracanti, J., Rabarison, M. K., Patrick, C., Baham, J. M., Young, J., et al. (2009). A simulation study of mesoscale coastal circulations in Mississippi Gulf Coast. *Atmospheric Research*, *91*(1), 9–25. https://doi.org/10.1016/j.atmosres.2008.05.004

Chen, F., & Dudhia, J. (2001). Coupling an advanced land surface-hydrology model with the Penn State-NCAR MM5 modeling system. Part I: Model implementation and sensitivity. *Monthly Weather Review*, *129*(4), 569–585. https://doi.org/10.1175/1520-0493(2001)129<0569:CAALSH>2.0.CO;2

Clappier, A., Martilli, A., Grossi, P., Thunis, P., Pasi, F., Krueger, B. C., et al. (2000). Effect of sea breeze on air pollution in the greater athens area. Part I: Numerical simulations and field observations. *Journal of Applied Meteorology and Climatology*, *39*, 546–562.

Comin, A. N., Miglietta, M. M., Rizza, U., Acevedo, O. C., & Degrazia, G. A. (2015). Investigation of sea-breeze convergence in Salento Peninsula (southeastern Italy). *Atmospheric Research*, *160*, 68–79. https://doi.org/10.1016/j.atmosres.2015.03.010

Couvreux, F., Bazile, E., Canut, G., Seity, Y., Lothon, M., Lohou, F., et al. (2016). Boundary-layer turbulent processes and mesoscale variability represented by numerical weather prediction models during the BLLAST campaign. *Atmospheric Chemistry and Physics*, *16*(14), 8983–9002. https://doi.org/10.5194/acp-16-8983-2016

Crosman, E. T., & Horel, J. D. (2010). Sea and lake breezes: A review of numerical studies. *Boundary-Layer Meteorology*, *137*(1), 1–29. https://doi.org/10.1007/s10546-010-9517-9

Cuxart, J., Conangla, L., & Jiménez, M. A. (2015). Evaluation of the surface energy budget equation with experimental data and the ECMWF model in the Ebro valley. *Journal of Geophysical Research: Atmospheres*, *113*, D12119. https://doi.org/10.1029/2007JD009583

de Haij, M., Wauben, W., & Klein Baltink, H. (2007). *Continuous mixing layer height determination using the ld-40 ceilometer: A feasibility study*. De Bilt: Royal Netherlands Meteorological Institute (KNMI).

de Roode, S. R., Bosveld, F. C., & Kroon, P. S. (2010). Dew formation, eddy correlation latent heat fluxes, and the surface energy imbalance at Cabauw during stable conditions. *Boundary-Layer Meteorol*, *135*(3), 369–383. https://doi.org/10.1007/s10546-010-9476-1

Deardorff, J. W. (1972). Numerical investigation of neutral and unstable planetary boundary layers. *Journal of the Atmospheric Sciences*, *29*(1), 91–115. https://doi.org/10.1175/1520-0469(1972)029<0091:NIONAU>2.0.CO;2

Dudhia, J. (1989). Numerical study of convection observed during the winter monsoon experiment using a mesoscale two-dimensional model. *Journal of the Atmospheric Sciences*, *46*, 3077–3107.

Dudhia, J. (1996). A multi-layer soil temperature model for MM5. In *Conference:Sixth annual psu/ncar mesoscale model users' workshop*, Boulder, Colorado.

Foken, T. (2008). The energy balance closure problem: An overview. *Ecological Applications*, *18*(6), 1351–1367. https://doi.org/10.1890/06-0922.1

Gangoiti, G., Millán, M. M., Salvador, R., & Mantilla, E. (2001). Long-range transport and re-circulation of pollutants in the western Mediterranean during the project Regional Cycles of Air Pollution in the West-Central Mediterranean Area. *Atmospheric Environment*, *35*(36), 6267–6276. https://doi.org/10.1016/S1352-2310(01)00440-X

Hernádez-Ceballos, M. A., Vargas, A., Arnold, D., & Bolívar, J. P. (2015). The role of mesoscale meteorology in modulating the 222rn concentrations in Huelva (Spain)—Impact of phosphogypsum piles. *Journal of Environmental Radioactivity*, *145*, 1–9. https://doi.org/10.1016/j.jenvrad.2015.03.023

Hong, S.-Y., & Lim, J.-O. (2006). The WRF single-moment 6-class microphysics scheme (WSM6). *Journal of the Korean Meteorological Society*, *42*, 129–151.

Hong, S.-Y., Noh, Y., & Dudhia, J. (2006). A new vertical diffusion package with an explicit treatment of entrainment processes. *Monthly Weather Review*, *134*, 2318–2341.

Hu, X.-M., & Xue, M. (2016). Influence of synoptic sea-breeze fronts on the urban heat island intensity in Dallas-Fort Worth, Texas. *Monthly Weather Review*, *144*(4), 1487–1507. https://doi.org/10.1175/MWR-D-15-0201.1

Hughes, C. P., & Veron, D. E. (2018). A characterization of the delaware sea breeze using observations and modeling. *Journal of Applied Meteorology and Climatology*, *57*(7), 1405–1421. https://doi.org/10.1175/JAMC-D-17-0186.1

Jiménez, P. A., de Arellano, J. V.-G., Dudhia, J., & Bosveld, F. C. (2016). Role of synoptic- and meso-scales on the evolution of the boundary-layer wind profile over a coastal region: the near-coast diurnal acceleration. *Meteorology and Atmospheric Physics*, *128*(1), 39–56. https://doi.org/10.1007/s00703-015-0400-6

Jiménez, M. A., Simó, G., Wrenger, B., Telisman-Prtenjak, M., Guijarro, J. A., & Cuxart, J. (2016). Morning transition case between the land and sea breeze regimes. *Atmospheric Research*, *172-173*, 95–108. https://doi.org/10.1016/j.atmosres.2015.12.019

Lothon, M., Lohou, F., Pino, D., Couvreux, F., Pardyjak, E. R., Reuder, J., et al. (2014). The BLLAST field experiment: Boundary-layer late afternoon and sunset turbulence. *Atmospheric Chemistry and Physics*, *14*(20), 10,931–10,960. https://doi.org/10.5194/acp-14-10931-2014

Meir, T., Orton, P., Pullen, J., Holt, T., Thompson, W. T., & Arend, M. F. (2013). Forecasting the New York City urban heat island and sea breeze during extreme heat events. *Weather Forecasting*, *28*, 1460–1477.

Mestayer, P. G., Calmet, I., Herlédant, O., Barré, S., Piquet, T., & Rosant, J.-M. (2018). A coastal bay summer breeze study, Part 1: Results of the Quiberon 2006 experimental campaign. *Boundary-Layer Meteorology*, *167*(1), 1–26. https://doi.org/10.1007/s10546-017-0314-6

Miller, S. T. K., Keim, B. D., Talbot, R. W., & Mao, H. (2003). Sea breeze: Structure, forecasting, and impacts. *Reviews of Geophysics*, *41*, 1–31. https://doi.org/10.1029/2003RG000124

Mlawer, E. J., Taubman, S., Brown, P., Iacono, M., & Clough, S. (1997). Radiative transfer for inhomogeneous atmosphere: RRTM, a validated correlated-k model for the longwave. *Journal of Geophysical Research*, *102*, 16,663–16,682.

Ogawa, S., Sha, W., Iwasaki, T., & Wang, Z. (2003). A numerical study on the interaction of a sea-breeze front with convective cells in the daytime boundary layer. *Journal of the Meteorological Society of Japan Ser. II*, *81*(4), 635–651. https://doi.org/10.2151/jmsj.81.635

Papanastasiou, D. K., Melas, D., Bartzanas, T., & Kittas, C. (2010). Temperature, comfort and pollution levels during heat waves and the role of sea breeze. *International Journal of Biometeorology*, *54*(3), 307–317. https://doi.org/10.1007/s00484-009-0281-9

Papanastasiou, D. K., Melas, D., & Lissaridis, I. (2010). Study of wind field under sea breeze conditions; an application of WRF model. *Atmospheric Research*, *98*(1), 102–117. Clouds, Aerosols and Radiation https://doi.org/10.1016/j.atmosres.2010

Ronda, R. J., & Bosveld, F. C. (2009). Deriving the surface soil heat flux from observed soil temperature and soil heat flux profiles using a variational data assimilation approach. *Journal of Applied Meteorology and Climatology*, *48*(3), 644–656. https://doi.org/10.1175/2008JAMC1930.1

Ruisdael-Observatory (2019). ruisdael-observatory.nl. Retrieved from ruisdael-observatory.nl/

SEDAC (2019). Gridded population of the world (gpw), v4. Retrieved from https://sedac.ciesin.columbia.edu/data/collection/gpw-v4

Salvador, N., Reis, N. C., Santos, J. M., Albuquerque, T. T. d. A., Loriato, A. G., Augustin, P., et al. (2016). Evaluation of Weather Research and Forecasting model parameterizations under sea-breeze conditions in a north sea coastal environment. *Journal of Meteorological Research*, *30*(6), 998–1018. https://doi.org/10.1007/s13351-016-6019-9

Sastre, M., Yagüe, C., Román-Cascón, C., & Maqueda, G. (2015). Atmospheric boundary-layer evening transitions: A comparison between two different experimental sites. *Boundary-Layer Meteorology*, *157*(3), 375–399.

Seroka, G., Fredj, E., Kohut, J., Dunk, R., Miles, T., & Glenn, S. (2018). Sea breeze sensitivity to coastal upwelling and synoptic flow using Lagrangian methods. *Journal of Geophysical Research: Atmospheres*, *123*, 9443–9461.

Soler, M. R., Udina, M., & Ferreres, E. (2014). Observational and numerical simulation study of a sequence of eight atmospheric density currents in northern Spain. *Boundary-Layer Meteorology*, *153*(2), 195–216. https://doi.org/10.1007/s10546-014-9942-2

Steele, C. J., Dorling, S. R., von Glasow, R., & Bacon, J. (2013). Idealized WRF model sensitivity simulations of sea breeze types and their effects on offshore windfields. *Atmospheric Chemistry and Physics*, *13*, 443–461.

Steeneveld, G. J., Tolk, L. F., Moene, A. F., Hartogensis, O. K., Peters, W., & Holtslag, A. A. M. (2011). Confronting the WRF and RAMS mesoscale models with innovative observations in the Netherlands: Evaluating the boundary layer heat budget. *Journal of Geophysical Research*, *116*, D23114. https://doi.org/10.1029/2011JD016303

Sun, X., Holmes, H. A., Osibanjo, O. O., Sun, Y., & Ivey, C. E. (2017). Evaluation of surface fluxes in the WRF model: Case study for farmland in rolling terrain. *Atmosphere*, *8*, 197. https://doi.org/10.3390/atmos8100197

Verkaik, J. W., & Holtslag, A. A. M. (2007). Wind profiles, momentum fluxes and roughness lengths at Cabauw revisited. *Boundary-Layer Meteorology*, *122*(3), 701–719. https://doi.org/10.1007/s10546-006-9121-1

Zahorowski, W., Williams, A. G., Vermeulen, A. T., Chambers, S. D., Crawford, J., & Sisoutham, O. (2008). Diurnal boundary layer mixing patterns characterised by radon-222 gradient observations at Cabauw, *Extended abstracts, 18th conf. on boundary layers and turbulence, stockholm, sweden*. Stockholm, Sweden: American Meteorological Society.

Zhong, S., In, H., & Clements, C. (2007). Impact of turbulence, land surface, and radiation parameterizations on simulated boundary layer properties in a coastal environment. *Journal of Geophysical Research*, *112*, D13110. https://doi.org/10.1029/2006JD008274